Caveolae promote successful abscission by controlling intercellular bridge tension during cytokinesis

Virginia Andrade, Jian Bai, Neetu Gupta-Rossi, Ana Joaquina Jimenez, Cédric Delevoye, Christophe Lamaze, Arnaud Echard

CELL BIOLOGY

Caveolae promote successful abscission by controlling intercellular bridge tension during cytokinesis

Virginia Andrade[1,2], Jian Bai[1,2], Neetu Gupta-Rossi[1], Ana Joaquina Jimenez[3], Cédric Delevoye[4,5], Christophe Lamaze[6], Arnaud Echard[1]*

During cytokinesis, the intercellular bridge (ICB) connecting the daughter cells experiences pulling forces, which delay abscission by preventing the assembly of the ESCRT scission machinery. Abscission is thus triggered by tension release, but how ICB tension is controlled is unknown. Here, we report that caveolae, which are known to regulate membrane tension upon mechanical stress in interphase cells, are located at the midbody, at the abscission site, and at the ICB/cell interface in dividing cells. Functionally, the loss of caveolae delays ESCRT-III recruitment during cytokinesis and impairs abscission. This is the consequence of a twofold increase of ICB tension measured by laser ablation, associated with a local increase in myosin II activity at the ICB/cell interface. We thus propose that caveolae buffer membrane tension and limit contractibility at the ICB to promote ESCRT-III assembly and cytokinetic abscission. Together, this work reveals an unexpected connection between caveolae and the ESCRT machinery and the first role of caveolae in cell division.

INTRODUCTION

Cytokinesis is the last step of cell division and physically separates the daughter cells. In animal cells, cytokinesis is driven by local and highly coordinated polymerization/depolymerization of different types of cytoskeleton and filaments (*1*, *2*). First, the ingression of the cleavage furrow depends on the contraction of an acto-myosin ring at the cell equator. Then, the intercellular bridge (ICB) connecting the daughter cells is stabilized by septins. Last, the midbody at the center of the ICB recruits the abscission machinery that pinches the membrane on one side of the midbody at the future abscission site (fig. S1A) (*2*). This last step requires the local disassembly of microtubules and actin filaments (*2*–*9*), as well as the timely polymerization of ESCRT-III (endosomal sorting complex required for transport III) filaments at the abscission site (*1*, *10*–*13*). The ESCRT-III–driven constriction of the plasma membrane eventually leads to the scission of the ICB (*1*, *2*).

What triggers ESCRT-III filament assembly at the right place and time, first at the midbody and then at the abscission site, remains poorly understood. While several biochemical components, such as CEP55, MKLP1, ALIX, TSG101, and Syndecan-4, are key for the proper recruitment, localization, and polymerization of the ESCRT-III machinery (*1*, *2*), it has been shown that mechanical inputs play a critical role as well. After furrow ingression, the daughter cells exert nanonewton-range pulling forces on the bridge, which is thus under tension (*14*). Rather than favoring abscission, this, on the contrary, delays ESCRT-III recruitment at the abscission site (*14*). It has thus been proposed that abscission requires a tension release in the ICB (*14*), but how this is controlled remains elusive. Understanding the regulation of the intercellular forces in the ICB should thus reveal one of the most upstream events that initiate abscission.

Here, we identified caveolae as a key regulator that limits ICB tension to promote abscission. Caveolae are characteristic cup-shaped 50- to 100-nm invaginations of the plasma membrane, discovered in the 1950s (*15*–*17*). The formation of caveolae requires two types of structural components: caveolins, which are partially embedded in the plasma membrane, and cavins, which form a coat around caveolae (*15*, *16*). In addition, accessory proteins such as EHD2 and PACSINS regulate caveolae dynamics (*15*–*17*). In vertebrates, caveolae are particularly abundant in cells that experience chronical mechanical constraints, such as muscle cells, endothelial cells, and adipocytes (*15*, *16*). Functionally, caveolae define nanometer-scale lipid compartments at the plasma membrane and have been involved in the regulation of many signaling events (*18*). Over the past decade, it also emerged that caveolae constitute a membrane reservoir that plays a critical role in buffering membrane tension in nondividing cells experiencing mechanical stress through their ability to flatten out (*19*–*22*). This is particularly important to maintain tissue integrity in adult tissues, during development and in pathological situations such as cancers (*23*–*28*).

Cells experience important forces and shape changes during cell division, but little is known about caveolae during mitosis or cytokinesis. At the onset of mitosis, before chromosome segregation, caveolin-1 (Cav1) is enriched at cortical regions and guides spindle orientation (*29*). Later, in metaphase, Cav1 redistributes from the plasma membrane to internal compartments, accompanied with fission of caveolae from the plasma membrane (*30*). Conversely, Cav1 reappears at the membrane during telophase in HeLa cells (*30*). Furthermore, it is known for long that Cav1 concentrates at the cleavage furrow in Madin-Darby canine kidney cells and in early zebrafish embryos (*31*, *32*). However, the significance of this dynamic redistribution of Cav1 during mitotic exit, and whether caveolae have a role in cell division, remains unknown.

Using a variety of approaches, from endogenous immunostaining, high-resolution spinning disk confocal microscopy, electron microscopy (EM), CRISPR-Cas9 knockout (KO) cells to laser ablation for measuring tension, we report that (i) bona fide caveolae are

[1]Institut Pasteur, Université Paris Cité, CNRS UMR3691, Membrane Traffic and Cell Division Unit, 25-28 rue du Dr Roux, F-75015 Paris, France. [2]Sorbonne Université, Collège doctoral, F-75005 Paris, France. [3]Dynamics of Intracellular Organization Laboratory, Institut Curie, PSL Research University, CNRS UMR 144, Sorbonne Université, 75005 Paris, France. [4]Institut Curie, PSL Research University, CNRS, UMR144, Structure and Membrane Compartments, 75005 Paris, France. [5]Institut Curie, PSL Research University, CNRS, UMR144, Cell and Tissue Imaging Facility (PICT-IBiSA), 75005 Paris, France. [6]Institut Curie, PSL Research University, INSERM U1143, CNRS UMR 3666, Membrane Mechanics and Dynamics of Intracellular Signaling Laboratory, 26 rue d'Ulm, 75005 Paris, France.
*Corresponding author. Email: arnaud.echard@pasteur.fr

present at the midbody and at the sides of the ICB after furrow ingression, (ii) caveolae regulate acto-myosin II–dependent contractility at the ICB and ICB mechanical tension, and (iii) by limiting ICB tension, caveolae promote both ESCRT-III assembly and abscission. This work thus reveals the first function of caveolae in cell division, whereby caveolae buffer tension in the ICB, a physical parameter that is critical for successful cytokinesis.

RESULTS

Caveolae are present at the midbody and at the ICB/cell interface

In many cell types, abscission occurs on both sides of the midbody and releases a midbody remnant (MBR; fig. S1A) (*14*, *33*–*36*). We recently developed a new method for isolating pure, intact MBRs from HeLa cells and provided the quantitative proteome of this organelle that we termed the Flemmingsome (*37*). Data analysis led to the intriguing discovery that several proteins constitutive of caveolae were either present (Cav1, PACSIN2, Cavin3, and EHD2) or enriched (Cavin1/PTRF and PACSIN3, >3.5-fold and >3-fold compared to control fractions, respectively) in the Flemmingsome (fig. S1B). In this study, we chose to focus on Cavin1 and Cav1, as both are essential structural components of caveolae (*15*, *16*).

Immunostaining of purified MBRs from HeLa cells expressing the midbody marker MKLP1–green fluorescent protein (GFP) showed endogenous Cavin1 and Cav1 localization on dotty structures (Fig. 1A and fig. S2A), consistent with the proteomic data. During cytokinesis, we also observed an accumulation of similar structures containing Cavin1 (Fig. 1B and fig. S2B) and Cav1 (fig. S2C) that were tightly juxtaposed to the plasma membrane marker Rab35 of the cytokinetic furrow when ingressed, as previously reported for Cav1 in other cell types (*31*, *32*). In addition, we found that both proteins localized to the midbody in 80 to 90% of both early and late ICBs [characterized by thick and thin tubulin staining, respectively (*33*, *37*)], which had not been reported thus far (Fig. 1B and fig. S2, B and C). The presence of Cavin1 dots juxtaposed or colocalized with the midbody ring markers RacGAP1 and CEP55 and the plasma membrane marker Rab35 suggested the existence of caveolae at the midbody, since Cavin1 at the plasma membrane is only present on fully budded caveolae (*17*). To determine whether bona fide caveolae were present at the midbody, we turned to EM. Using scanning EM (SEM), we observed small open structures at the midbody ring that likely correspond to membrane invaginations (Fig. 1C, arrows). Transmission EM (TEM) on ultrathin two-dimensional sections further demonstrated the presence at the midbody of small (50 to 100 nm) plasma membrane invaginations without electron-dense coat and that have the typical morphology of caveolae (Fig. 1D, arrow).

After furrow ingression, we also frequently observed an accumulation of dotty Cavin1- and Cav1-positive structures at one or both sides of the ICB (Fig. 1E and fig. S2D). These flanking regions of the ICB correspond to the interface between the ICB and the daughter cell, and we thus named them "entry points" (EPs). TEM confirmed that caveolae were present at the plasma membrane at the EPs (Fig. 1F, arrows). In late cytokinetic bridges, secondary constrictions with decreased microtubule staining are found ~1 μm away from midbody and correspond to the tip of the ESCRT-III cone that constricts at the presumptive abscission site (see fig. S1A) (*4*, *33*, *37*). The accumulation of caveolae at EPs was observed in approximately 40% of late ICBs without secondary constrictions but only in 10% of ICBs with secondary constrictions (which correspond to ICBs temporally closer to abscission) (Fig. 1E and fig. S2D). This indicates that the number of caveolae at the EPs decreases as cells progress toward abscission. Together, we conclude that bona fide caveolae are present at the midbody and transiently at the ICB/cell interface after furrow ingression.

Cavin1 and Cav1 dynamically colocalize at the midbody and at the ICB/cell interface

To reveal the dynamics of the caveolae during cytokinesis, we monitored their localization in live cells using time-lapse spinning disk confocal microscopy in cells expressing both Cav1–red fluorescent protein (RFP) and Cavin1-GFP. As shown in Fig. 2A and movie S1, punctate structures positive for both Cavin1 and Cav1 localized at the ingressed furrow (190 min before abscission, time −190 min). As the ICB matured, pools of Cavin1 and Cav1 were found at the midbody (Fig. 2A, brackets, times −120, −70, and 0 min) and accumulated at EPs (Fig. 2A, squared regions, time −160 min). Quantification of Cavin1-GFP intensity at EPs (Fig. 2B, fig. S3A, and movie S2) revealed that (i) one EP is consistently more labeled than the other, suggesting an asymmetry in caveolae localization at EPs; (ii) Cavin1 intensity starts to decrease at both EPs approximately 100 min before abscission, with a sharper decrease 50 min before abscission; and (iii) abscission occurs approximately 20 min after both EPs have reached their minimal Cavin1 intensity. Since ESCRT-III starts to polymerize as a cone from the midbody toward the abscission approximately 30 min before abscission (see fig. S1A) (*37*), ESCRT-III polymerization is thus concomitant with low levels of Cavin1 at EPs. Cavin1-positive dots detected in live cell imaging were almost always positive for Cav1 (Fig. 2A, bottom), indicating that they correspond to caveolae (*15*–*17*), which is consistent with our EM data in fixed cells. Spinning disk confocal microscopy movies at 1-min interval acquisitions with Z-stacks further allowed us to monitor the fluorescence of individual Cavin1-GFP dots at EPs over time (fig. S2B). From randomly chosen caveolae dots that we could track, we often observed a progressive decrease in signal over several minutes until the dots fully disappeared and the Cavin1 signal reached the local background level (fig. S3B, first four examples). This raises the possibility that the global decrease of Cavin1 signal at EPs relies, at least in part, on the progressive flattening of caveolae.

Beside the midbody and EPs, we also noticed the presence of discrete Cavin1- and Cav1-positive punctate structures at the future abscission site (fig. S3C, arrowheads). These structures contained both Cavin1 and Cav1 and were localized at the distal tip (Fig. 2C, arrowhead) of the ESCRT-III cone labeled by CHMP4B (Fig. 2C, arrow). Time-lapse microscopy demonstrated that this pool of caveolae becomes visible at the same time as the ESCRT-III cone starts to polymerize (observed in 9 of 11 cones). This pool always and quickly disappeared (in 15.5 ± 5.3 min, mean ± SD), while the ESCRT-III cone continued to polymerize toward the abscission site (Fig. 2D).

In summary, caveolae are found at the midbody throughout cytokinesis. They are also found at the ICB/cell interface (i.e., EPs) and at the tip of the ESCRT-III machinery, and progressively disappear from these locations as cells progress toward abscission.

Loss of caveolae impairs abscission and ESCRT-III localization

To investigate the function of caveolae in cytokinesis, we took advantage of a HeLa cell line KO for Cavin1 that we recently generated

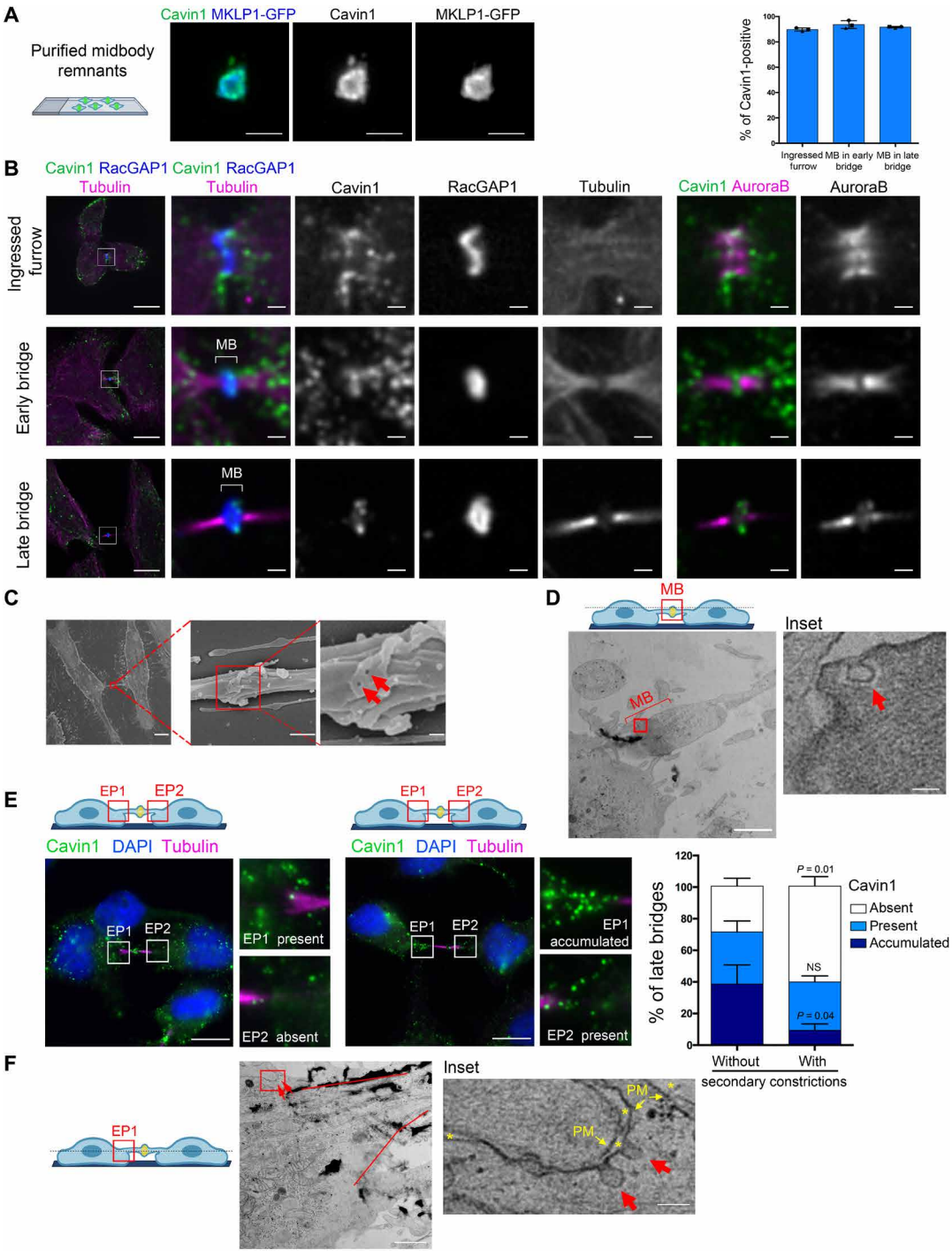

Fig. 1. Caveolae are present at the midbody and at the EPs during cytokinesis. (**A**) Purified midbody remnants from HeLa cells that stably express MKLP1-GFP were immunostained for endogenous Cavin1. Scale bars, 2 μm. (**B**) Left: Localization of endogenous Cavin1 in HeLa cells stained with α-tubulin + acetylated tubulin (hereafter "Tubulin"), RacGAP1, AuroraB, and 4′,6-diamidino-2-phenylindole (DAPI) at the indicated stages of cytokinesis. Scale bars, 10 μm (general views) and 1 μm (insets of the boxed regions). Top right: Percentage of the indicated structures positive for endogenous Cavin1. Mean ± SD, $n > 20$ cells per condition. $N = 3$ independent experiments. (**C**) Scanning EM pictures of an ICB (left) and midbody at different magnifications (successive insets). Red arrows point to membrane invaginations. Scale bars, 10 μm (left), 500 nm (middle), and 100 nm (right). (**D**) TEM pictures of a midbody, with inset showing caveolae (red arrow). Scale bars, 10 μm (left) and 100 nm (inset). (**E**) Left and middle: Two examples of endogenous staining for Cavin1, together with Tubulin and DAPI, in late bridges. Insets show different categories of Cavin1 localization at EPs. Scale bars, 10 μm. Right: Percentage of late bridges with/without secondary constriction where Cavin1 is accumulated, present or absent at EPs, as indicated. Mean ± SD, $n > 30$ cells per condition. $N = 3$ independent experiments. One-sided Student's t tests. NS, nonsignificant ($P > 0.05$). (**F**) TEM pictures of an EP region, with the ICB highlighted with red lines and caveolae marked with red arrows. The inset shows caveolae (red arrows) connected to the plasma membrane (PM) and facing the extracellular space (asterisks). Scale bars, 10 μm and 100 nm (inset).

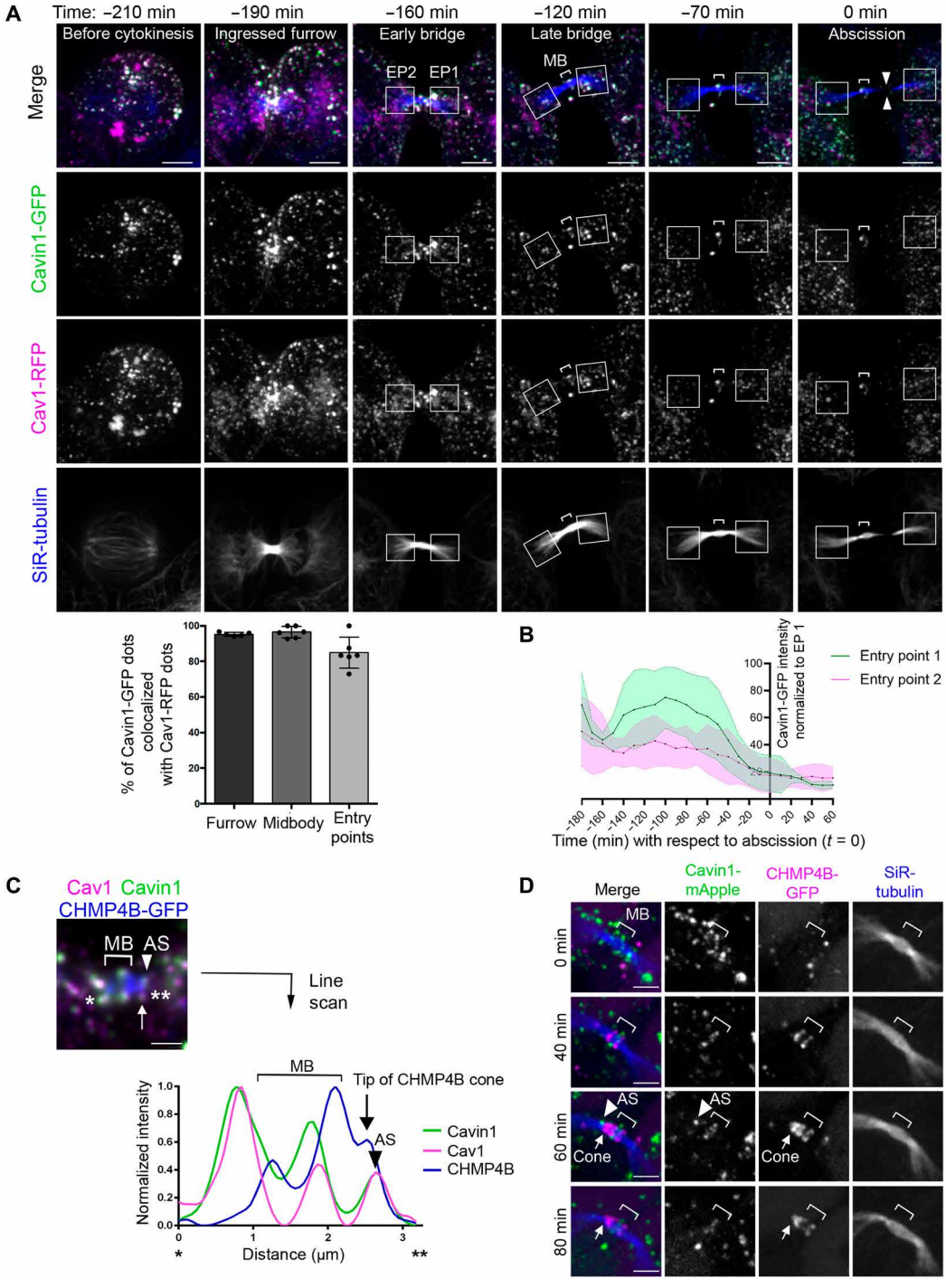

Fig. 2. Cavin1 and Cav1 dynamically colocalize at the midbody, the EPs, and the abscission site. (**A**) Top: Snapshots of a spinning disk confocal microscopy movie of cells coexpressing Cavin1-GFP and Cav1-RFP and incubated with SiR-tubulin. Squares: EPs. Brackets: Midbodies. Facing arrowheads: Abscission site. Time 0 indicates the time of abscission. Note the progressive disappearance of Cavin1/Cav1 in EP regions as cells progress to abscission. Scale bars, 5 μm. Bottom: Percentage of Cavin1-GFP dots colocalizing with Cav1-RFP dots at the furrow, midbody, and EPs. Mean ± SD, $n = 6$ movies of dividing cells. (**B**) Intensity of Cavin1-GFP staining as a function of time at EP1 and EP2 in $n = 10$ cells throughout cytokinesis (see representative video in fig. S3A). The brightest EP was defined as EP1, and the values of EP1 (green) and EP2 (magenta) were normalized to the maximum intensity observed in EP1 during cytokinesis for each cell analyzed. All movies were registered with respect to the time of abscission ($t = 0$). Mean ± SD, $n = 10$ movies. (**C**) Top: Endogenous staining for Cav1 and Cavin1 in cells stably expressing CHMP4B-GFP, with a zoom centered on the ICB. Arrow: CHMP4B-GFP polymerizing cone. Arrowhead: Abscission site (AS). Note the colocalization of Cavin1/Cav1 at the ICB/midbody and at the abscission site. Bottom: Intensity profiles between * and ** along the bridge of the merged picture. Scale bars, 1 μm. (**D**) Snapshots of a spinning disk confocal microscopy movie of a cell expressing Cavin1-mApple and CHMP4B-GFP incubated with SiR-tubulin. Arrow: CHMP4B-GFP polymerizing cone. Note that the green Cavin1 dot at the tip of the CHMP4B cone disappears while the cone constricts the microtubules at the future abscission site. Scale bars, 2 μm.

using CRISPR-Cas9 strategy (*38*). Western blots confirmed the absence of Cavin1 protein expression in these cells (Fig. 3A). In addition, we observed the complete disappearance of Cavin1 dots by immunofluorescence (fig. S4A). As expected, this was accompanied with a strong reduction of Cav1-positive dots upon Cavin1 KO (fig. S4B), since Cavin1 and Cav1 protein levels are correlated (*39*, *40*). Using TEM, we did not detect the presence of caveolae profiles in Cavin1 KO cells, neither in interphase cells nor in cytokinetic cells, contrary to Control KO cells (Fig. 3B, arrows, and fig. S4, C and D, for the corresponding regions at low magnification). We conclude that caveolae are absent in the Cavin1 KO cells that we generated.

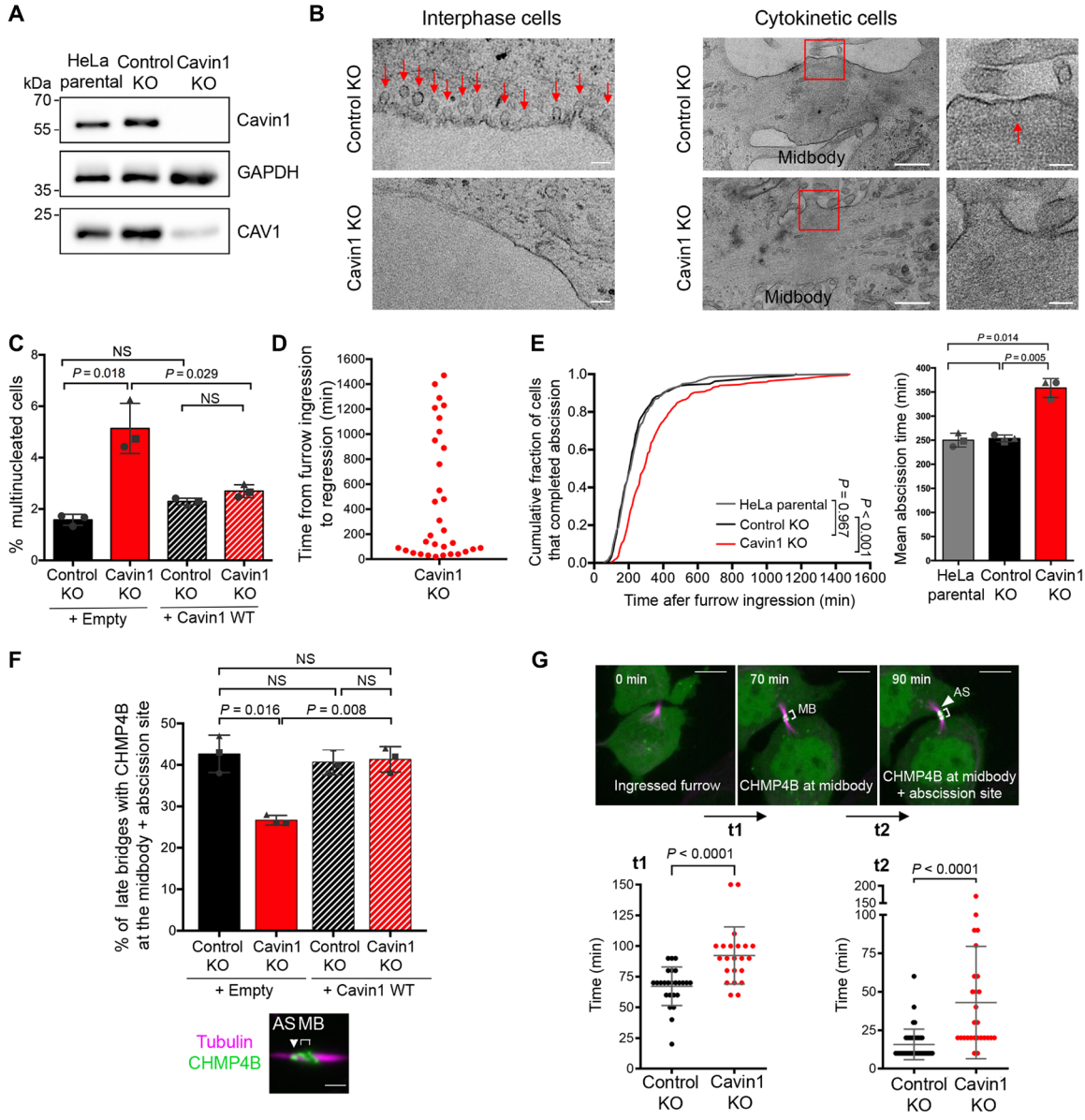

Fig. 3. Depletion of Cavin1 impairs ESCRT-III localization and abscission. (**A**) Lysates of parental HeLa, Control KO, and Cavin1 KO cells were blotted for Cavin1, Cav1, and GAPDH (glyceraldehyde-3-phosphate dehydrogenase) (loading control). (**B**) TEM micrographs of ultrathin sections of Control KO and Cavin1 KO cells in interphase (left; scale bars, 100 nm) and in cytokinesis (right; scale bars, 500 and 100 nm for insets). Red arrows: Caveolae profiles observed only in Control KO cells. See fig. S4 (C and D) for full fields of view and quantifications. (**C**) Percentage of bi-/multinucleated cells in indicated cells. Mean ± SD, $n > 500$ cells per condition. $N = 3$ independent experiments. (**D**) Time from the start of furrow ingression to furrow/bridge regression in the Cavin1 KO cells that became binucleated ($n = 32$ cells). (**E**) Left: Cumulative distribution of the fraction of cells that completed abscission, measured by phase-contrast time-lapse microscopy in indicated cells. Kolmogorov-Smirnov tests. Right: Mean abscission times (min) ± SD in indicated cells, with $n > 60$ cells per condition. $N = 3$ independent experiments. (**F**) Proportion of late cytokinetic bridges with endogenous CHMP4B localized both at the midbody and at the abscission site (see representative image) in indicated cells. Mean ± SD, $n > 30$ cells per condition. $N = 3$ independent experiments. Scale bar, 2 μm. (**G**) Top: Control KO and Cavin1 KO cells stably expressing CHMP4B-GFP were recorded by spinning disk confocal time-lapse microscopy. t1: Time from cleavage furrow ingression ($t = 0$ min) to CHMP4B-GFP recruitment at the midbody; t2: Time from CHMP4B-GFP at the midbody to CHMP4B-GFP at midbody + abscission site. Scale bars, 5 μm. Bottom: t1 and t2 (min) ± SD. $n > 23$ cells. $N = 4$ independent experiments. Two-sided (C, E, and F) and unpaired (G) Student's *t* tests. NS, nonsignificant ($P > 0.05$).

Most noteworthy, the lack of caveolae was associated with a threefold increase in the number of multinucleated cells in the Cavin1 KO cell population (Fig. 3C). Using time-lapse phase-contrast microscopy, we observed that these binucleated cells arose from a regression of the furrow after its complete ingression, most often after the normal time of abscission (median abscission time is 210 min in control cells) (Fig. 3D), suggesting abortive cytokinesis after abscission defects. Confirming this hypothesis, abscission was delayed in Cavin1 KO cells compared to control cells (Fig. 3E). Reexpression of Cavin1 in the KO cells fully rescued the cytokinetic defects, ruling out off-target artifacts (Fig. 3C and fig. S5A). Similarly, depletion of Cav1 by small interfering RNAs (siRNAs) resulted in the loss of Cav1-positive structures (fig. S5B) and delayed abscission as well (fig. S5C).

To understand the origin of the abscission defects induced by the loss of caveolae, we next investigated the ESCRT scission machinery by monitoring the key ESCRT-III subunit CHMP4B. In fixed cells, Cavin1 KO led to a decrease in the proportion of ICBs with CHMP4B both at the midbody and at the abscission site (Fig. 3F). This suggested a defect in ESCRT-III assembly at the abscission site upon removal of caveolae. As expected, the abnormal localization of CHMP4B was fully rescued by reexpressing Cavin1 (Fig. 3F). Spinning disk confocal microscopy further demonstrated delayed arrival of CHMP4B-GFP both at the midbody (t1; Fig. 3G) and at the abscission site (t2; Fig. 3G) upon Cavin1 KO. These results indicate that caveolae are required for the proper assembly of ESCRT-III at the midbody and at the abscission site. Together, this explains the abscission defects observed upon caveolae loss.

Caveolae limit acto-myosin II contractility at the ICB/cell interface and control ICB tension during cytokinesis

High tension in ICBs during cytokinesis delays ESCRT-III polymerization (*14*). Since membrane tension was found to contribute to half of the bridge tension (*14*) and caveolae can buffer membrane tension in interphase cells (*20*, *41*), we hypothesized that the loss of caveolae may increase ICB tension during cytokinesis. Changes in ICB tension can be measured by laser ablation. When the ICB is transversally cut by an ultraviolet (UV) laser (Fig. 4A), the initial speed of retraction was previously shown to be proportional to the forces exerted by the daughter cells on their ICB (*14*). Using this approach, we found a twofold increase of ICB tension in Cavin1 KO cells compared to Control KO cells (Fig. 4B and movie S3). Despite a wide range of ICB lengths, there was no correlation between ICB lengths and retraction speeds, both in Control KO and in Cavin1 KO cells (fig. S6A). This indicates that differences in tension at the ICB are not linked to ICB lengths and that increased tension in Cavin1 KO cells reflects higher forces exerted to the ICB in these cells. Furthermore, these results demonstrate that caveolae are functionally required to limit the ICB tension during cytokinesis.

Tension measured in the ICB can result from an entangled combination of membrane tension and cell contractility transmitted to the ICB by the acto-myosin system (*42*). We thus examined the activity of myosin II by measuring the levels of phosphorylated myosin II regulatory light chain (pMRLC) and F-actin localization upon Cavin1 depletion. First, we observed that the proportion of cytokinetic cells with F-actin accumulation at both EPs increased in Cavin1 KO cells (Fig. 4C). Conversely, the proportion of cytokinetic cells without F-actin accumulation at either EPs decreased in Cavin1 KO cells (Fig. 4C). Second, as seen for F-actin, the proportion of cytokinetic cells with accumulation of endogenous pMRLC at both EPs increased in Cavin1 KO cells (Fig. 4D). Conversely, the proportion of cytokinetic cells without pMRLC accumulation at either EPs decreased in Cavin1 KO cells (Fig. 4D). However, neither the total levels of MRLC nor the percentage of activated myosin II (ratio pMRLC/total MRLC) was changed in Cavin1 KO cells synchronized in cytokinesis (fig. S6B). Together, the loss of caveolae results in a higher proportion of ICBs displaying F-actin and activated myosin II in the EP regions.

Accumulation of F-actin at the ICB or close to the ICB can be observed when the abscission checkpoint (also known as the NoCut checkpoint) is activated, in particular in the abnormal presence of chromatin bridges within ICBs (*43*–*46*). However, several lines of evidence indicate that the accumulation of F-actin and the delayed abscission are not a consequence of the activation of the abscission checkpoint in Cavin1 KO cells. We observed that (i) the proportion of ICBs with chromatin bridges was not increased upon Cavin1 depletion (fig. S7A); (ii) the translocation of activated AuroraB (phosphorylated pT232 AuroraB) at the midbody ring—a hallmark of the activation of the checkpoint associated with actin accumulation (*43*)—was not observed in the dividing Cavin1 KO cells that did not display chromatin bridges (fig. S7B) and that represent the vast majority of the cytokinetic cells (fig. S7A); (iii) the levels of monophosphorylated CHMP4C (pCHMP4C) at the midbody did not increase in Cavin1 KO cells—CHMP4C is a key component that is phosphorylated upon checkpoint activation (*13*, *47*–*49*) and accumulates at the midbody, for instance, after sister chromatid decatenation defects (fig. S7C) (*50*); and (iv) cytoplasmic "abscission checkpoint bodies" (ACBs) labeled by triple-phosphorylated CHMP4C (pppCHMP4C)—which are strongly induced by the activation of the abscission checkpoint by nuclear pore defects (*13*, *51*)—were not induced in Cavin1 KO cells (fig. S7D). As discussed below, we propose that a transient accumulation of F-actin and myosin II is a consequence of cell spreading in late telophase, independently of the activation of the abscission checkpoint. This accumulation persists upon caveolae depletion since ICB tension/myosin II activation cannot be buffered anymore.

In wild-type (WT) cells, we observed that structures with high levels of activated myosin II and high levels of Cavin1 were inversely correlated (and often mutually exclusive) within EP regions: At a local (i.e., pixel-size) scale, high-intensity Cavin1-positive structures (Fig. 4E, green peaks, and Fig. 4F, box b) were negative or weak for pMRLC (Fig. 4E, magenta peaks, and Fig. 4F, box b) and vice versa (Fig. 4E; Fig. 4F, box a; and fig. S8A for additional examples). At a broader (i.e., EP-size) scale, Cavin1 accumulated preferentially at EPs with no or little pMRLC, and conversely, pMRLC accumulated at EPs with no or little Cavin1 (fig. S8B). These observations suggest that the presence of caveolae locally restricts myosin II activation at EPs during cytokinesis, a hypothesis consistent with increased pMRLC at EPs found in the absence of Cavin1. Together, we conclude that the presence of caveolae limits both the presence of F-actin/active myosin II at the cell/ICB interface and the ICB tension during cytokinesis.

Increased ICB tension is responsible for the cytokinetic defects induced by the loss of caveolae

Our data raised the possibility that, upon Cavin1 depletion, the local increase in F-actin and activated myosin II at EPs could contribute to the observed increase in ICB tension, thus explaining the defects in ESCRT-III assembly and the abscission delay. To test this hypothesis,

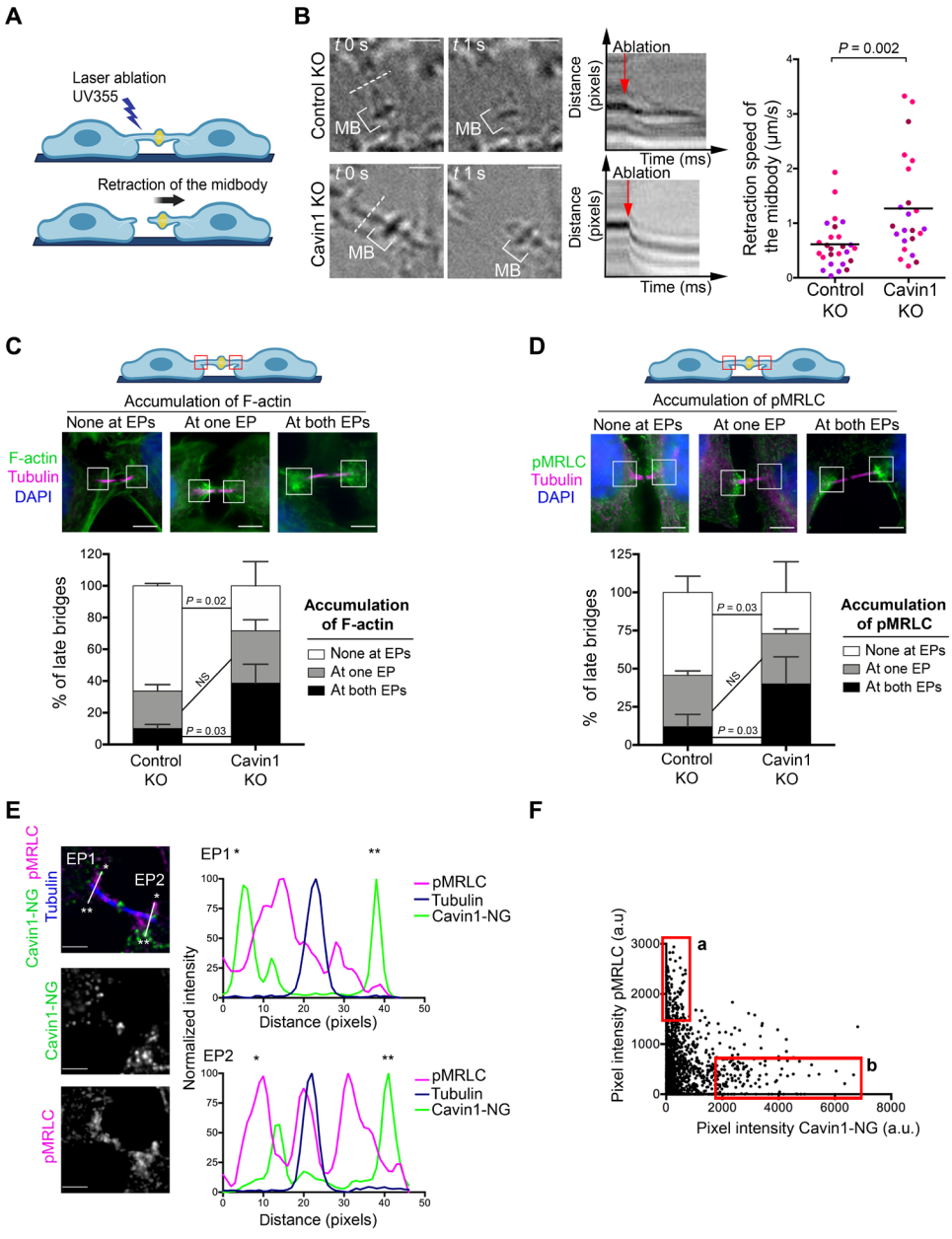

Fig. 4. Caveolae limit acto-myosin II at the EPs and control ICB tension during cytokinesis. (**A**) Scheme illustrating the laser ablation experiment. (**B**) Left: Snapshots of ICBs from Control KO and Cavin1 KO cells, before (t0) and after the laser ablation (t0 + 1 s) with corresponding kymographs (red arrows mark the moment of ablation). Dotted line: Position of the laser cut. Scale bars, 2 µm. Right: Retraction speed (micrometers per second) of midbodies in Control KO and Cavin1 KO ablated bridges. Horizontal bar: Mean, $n = 23$ to 24 ICBs from $N = 3$ independent experiments. Unpaired Student's t tests. (**C**) Top: Representative images of the three categories of endogenous F-actin staining (fluorescent phalloidin) accumulation in late ICBs: none at EPs, at one EP, and at both EPs. Scale bars, 5 µm. Bottom: Percentage of late bridges for each F-actin category. Mean ± SD, $n > 20$ cells per condition. $N = 3$ independent experiments. (**D**) Top: Representative images of the three categories of endogenous pMRLC staining accumulation in late ICBs: none at EPs, at one EP, and at both EPs. Scale bars, 5 µm. Bottom: Percentage of late bridges for each pMRLC category. Mean ± SD, $n > 30$ cells per condition. $N = 3$ independent experiments. (**E**) Left: Endogenous pMRLC and Tubulin staining in a Cavin1-NeonGreen (NG) stable cell line, with a zoom centered on the ICB. Scale bars, 2 µm. Right: Intensity profiles of the EP1 and EP2 regions. (**F**) Pixel intensity of pMRLC (y axis) and Cavin1-NG (x axis) at EP1 and EP2 from (E). Box a: High pMRLC/low Cavin1 intensity pixels. Box b: High Cavin1/low pMRLC intensity pixels. In (C) and (D), paired Student's t tests. NS, nonsignificant ($P > 0.05$). a.u., arbitrary units.

we treated Cavin1 KO cells with Y27632, a pharmacological inhibitor of ROCK, a kinase that activates myosin II through direct phosphorylation of MRLC. Upon ROCK inhibition, the increase in the proportion of ICBs with both EPs positive for pMRLC observed in Cavin1 KO cells was abolished (Fig. 5A). Concomitantly, ROCK inhibition restored ICB tension to normal levels in Cavin1 KO cells (Fig. 5B), suggesting that activated myosin II at EPs contributes to the ICB tension increase measured upon Cavin1 depletion. Notably, we selected a concentration of Y27632 (20 µM) that was sufficient to reestablish a normal ICB tension in Cavin1 KO cells but that was

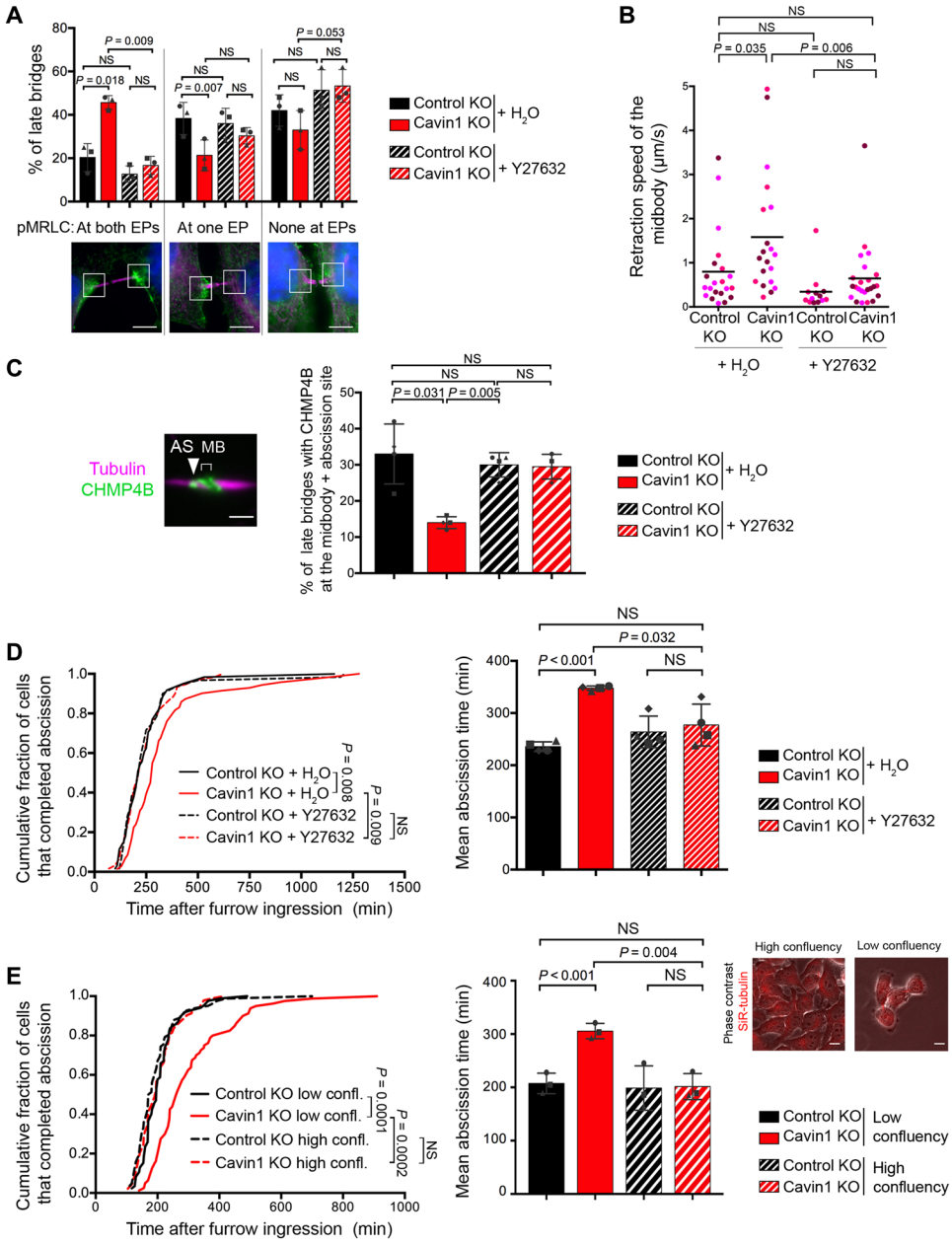

Fig. 5. Increased ICB tension upon Cavin1 depletion is responsible for the cytokinetic defects. (**A**) Quantification of pMRLC localization at the EPs as in Fig. 4D (same representative pictures; scale bars, 5 µm) in indicated cells, treated or not with the ROCK inhibitor Y27632. Mean ± SD, $n > 30$ cells per condition. $N = 3$ independent experiments. (**B**) Retraction speed (micrometers per second) of midbodies in Control KO and Cavin1 KO ablated bridges, treated or not with the ROCK inhibitor Y27632. Horizontal bar: Mean, $n > 12$ ICBs from $N = 3$ independent experiments. (**C**) Endogenous CHMP4B localization was quantified as in Fig. 3F (same representative picture; scale bar, 2 µm) in indicated cells, treated or not with the ROCK inhibitor Y27632 (no synchronization). Mean ± SD, $n > 30$ cells per condition. $N = 3$ independent experiments. (**D**) Left: Cumulative distribution of the fraction of cells that completed abscission, measured by phase-contrast time-lapse microscopy in indicated cells, treated or not with the ROCK inhibitor Y27632. Right: Mean abscission times (min) ± SD in indicated cells, with $n > 60$ cells per condition. $N = 4$ independent experiments. (**E**) Left: Cumulative distribution of the fraction of cells that completed abscission, measured by phase-contrast time-lapse microscopy in Control KO and Cavin1 KO cells, plated at low versus high confluency (see Materials and Methods). Middle: Mean abscission times (min) ± SD in indicated cells, with $n > 24$ cells per condition. $N = 3$ independent experiments. Right: Representative pictures of cells in low versus high confluency. Phase contrast (gray) and SiR-tubulin (red) are overlaid. Scale bars, 5 µm. Paired (A, C, D, and E) and unpaired (B) Student's *t* tests. Kolmogorov-Smirnov tests for cumulative curves (D and E). NS, nonsignificant ($P > 0.05$).

too low to abolish ICB tension in Control KO cells [in contrast to the 100 µM concentration used in other studies (*14*)]. In addition, 20 µM Y27632 did not affect early steps of cytokinesis—furrow ingression always occurred and took the same time in control cells treated or not with Y27632, 16 min ($n = 45$ cells) and 17 min ($n = 41$ cells), respectively ($P = 0.55$, *t* test). The treatment of Cavin1 KO cells with Y27632 was also sufficient to restore the correct assembly of ESCRT-III at the abscission site, whether Y27632 was present

throughout mitosis/cytokinesis (Fig. 5C) or whether it was added after furrow ingression for 2 hours (fig. S8C). Furthermore, reducing membrane tension by incubating the cells in a moderately hypertonic medium (400 mOsm) also restored the proper assembly of ESCRT-III at the abscission site in Cavin1 KO cells (fig. S9A). This treatment abolished the increase in the proportion of ICBs with both EPs positive for pMRLC, observed in Cavin1 KO cells (fig. S9B), highlighting the tight link between membrane tension and contractility (see Discussion). Collectively, these results show that reducing membrane tension or acto-myosin II–dependent contractility is sufficient to correct the abnormal localization of ESCRT-III at the abscission site observed upon the loss of caveolae. Accordingly, Y27632 treatment also rescued the abscission defects observed in Cavin1 KO cells (Fig. 5D). As another way to manipulate ICB tension, we cultured Cavin1 KO cells at high confluency (without inhibiting ROCK), a situation known to reduce ICB tension since the cytokinetic cells cannot pull as much on their ICB (*14*). Decreasing ICB tension by this means was also sufficient to prevent the abscission delay observed in Cavin1 KO cells cultured at lower confluency (Fig. 5E). These results independently confirm that caveolae promote abscission by reducing ICB tension. Noteworthy, in WT cells, we observed that the polymerization of ESCRT-III at the abscission site occurs concomitantly with a decrease in the accumulation of pMRLC at EPs (fig. S9C). This suggests that during normal cytokinesis, the drop in ICB tension known to promote abscission (*14*) relies on the decrease of acto-myosin II contractility at EPs, which is dependent on the presence of caveolae.

We conclude that the increase of tension in the ICB induced by the absence of caveolae is the cause of the defects in ESCRT-III assembly, which, in turn, impairs normal abscission. Therefore, caveolae are functionally required to promote ESCRT-III polymerization and successful abscission by limiting ICB tension during cytokinesis.

DISCUSSION

The decrease in ICB tension after furrow ingression is one of the most upstream mechanical determinants that control the assembly of the abscission machinery. However, no regulator of ICB tension other than myosin II has been reported so far. Here, we establish the first functional role of caveolae in cell division, which were found to buffer ICB tension to promote cytokinetic abscission.

Our recent proteomic analysis of MBRs purified by flow cytometry revealed the presence or the enrichment of several structural and regulatory components of caveolae (Cav1, Cavin1, Cavin3, EHD2, PACSIN2, and PACSIN3) (fig. S1B). The compilation of other proteomic studies (*36*, *52*, *53*) of either ICBs or MBRs released into the culture medium confirmed this finding. This led us to hypothesize that caveolae could play an active role during cytokinesis. Proteins involved either in furrow ingression or in late cytokinetic stages often accumulate at the midbody and can be identified by mass spectrometry in purified MBRs (*36*, *37*, *52*). This recently allowed us to reveal the role of ALIX/syntenin/Syndecan-4 and BST2/tetherin in abscission and post-abscission MBR capture, respectively (*37*, *54*).

While a role of caveolae in cytokinesis has not been reported so far, the structural caveolae component Cav1 had been previously localized at the furrow (*31*, *32*). We confirmed and extended these observations using endogenous staining for both Cav1 and Cavin1 (Fig. 1B and fig. S2, B and C) as well as fluorescently tagged proteins (Fig. 2A). We also revealed the presence of caveolae components (i) at the midbody itself; (ii) at the EPs, which correspond to the interfaces between the ICB and the daughter cells (Figs. 1E and 2A and figs. S2D and S3A); and (iii) at the tip of the ESCRT-III cone while polymerizing toward the abscission site (Fig. 2, C and D). The extensive colocalization between Cavin1 with Cav1 in these structures (Fig. 2A) and with a plasma membrane marker (fig. S2B), together with EM data (Fig. 1, D and F), demonstrated that these are bona fide caveolae present at the plasma membrane. To our knowledge, the presence of caveolae had not been noticed in previous ultrastructural studies of cytokinesis such as (*55*–*58*). However, a careful inspection of the published EM micrographs suggests that caveolae profiles were also present [e.g., figure 5F, c and d, in (*56*); figure S2 0 nm in (*57*); and figures 1F, 3E, and 6D in (*58*)].

What could determine the localization of caveolae at these specific locations during cytokinesis? Intense recycling of caveolae components during mitotic exit and telophase has been reported (*30*), and it is thus possible that this contributes to the localization of caveolae at the cytokinetic furrow, EPs, and midbody. Alternatively, individual caveolae could diffuse from the cell body to the furrow, EPs, and midbody within the plane of the plasma membrane. Last, caveolae could also form in situ because of the peculiar lipid composition of the furrow and midbody membrane that is known to promote caveolae formation in nondividing cells (*59*–*63*). We also noticed that caveolae are particularly abundant at EPs when the plasma membrane adopts a funnel shape (as in Fig. 1E, "EP1 accumulated" right panels), possibly indicating that specific curvature might favor caveolae formation or retention. Regarding the intriguing presence of caveolae at the tip of the ESCRT-III cone, we noticed that the ESCRT-III subunit CHMP4B had been found in complex with several caveolae components (Cavin1, Cav1, and PACSIN3) using mass spectrometry (*64*). This could provide a molecular connection explaining the remarkable coupling between caveolae and ESCRT-III at the abscission site.

What is the role of caveolae during cytokinesis? Following furrow ingression, daughter cells exert nanonewton-range pulling forces on the ICB that must be reduced to favor abscission (*14*). Accordingly, high tension inhibits ESCRT-III polymerization at the abscission site during cytokinesis (*14*) and impairs CHMP4B recruitment and polymerization on membranes in vitro (*65*). Our results point to a key role of caveolae in limiting ICB tension, which, in turn, promotes ESCRT-III polymerization and consequently abscission. The depletion of Cavin1 results in (i) a twofold increase in ICB tension (Fig. 4B), (ii) a delay in ESCRT polymerization at the midbody and at the abscission site (Fig. 3, F and G), and (iii) a delay in abscission (Fig. 3E) or cytokinetic failure due to cytokinesis abortion, especially in cells with old bridges (Fig. 3, C and D). In addition, Cav1 depletion leads to similar defects in cytokinesis (fig. S5C). The increase in ICB tension upon caveolae loss is the cause of the cytokinetic failure, since decreasing membrane tension through a moderate hyperosmotic shock (fig. S9A) or by decreasing acto-myosin II–dependent contractility through ROCK inhibition (Fig. 5C and fig. S8C) restores the proper polymerization of ESCRT-III at the abscission site in Cavin1 KO cells. ROCK inhibition or high confluency conditions known to reduce ICB tension also rescue the abscission defects in these cells (Fig. 5, D and E). Thus, caveolae critically regulate ICB tension during cytokinesis.

How could caveolae control ICB tension during cytokinesis? ICB tension results from a combination of membrane tension and

cortical tension due to acto-myosin II–dependent contractility exerted on the ICB (*14*, *42*). We envision two, nonmutually exclusive, mechanisms to explain how caveolae might control both components of ICB tension.

First, the pool of caveolae present at the EPs could contribute to the decrease in membrane tension at the ICB by flattening out, as shown previously in nondividing cells (*19*, *42*). Consistently, using both fixed cells, 10-min and 1-min frequency time-lapse microscopy, we found that caveolae gradually disappeared from EPs as cells progressed through abscission (Figs. 1E and 2, A and B, and figs. S2D and S3A), possibly by progressive flattening (fig. S3B). Notably, long-lived caveolae (2 to 7 min) have been recorded previously and correspond to a small fraction of caveolae outside EP regions recorded by total internal reflection fluorescence (TIRF) microscopy (*30*, *62*, *66*). The accumulation of caveolae precisely at the interface between the ICB and the cell body would constitute a membrane reservoir ideally located for reducing membrane tension at the ICB. The caveolae-mediated membrane tension reduction

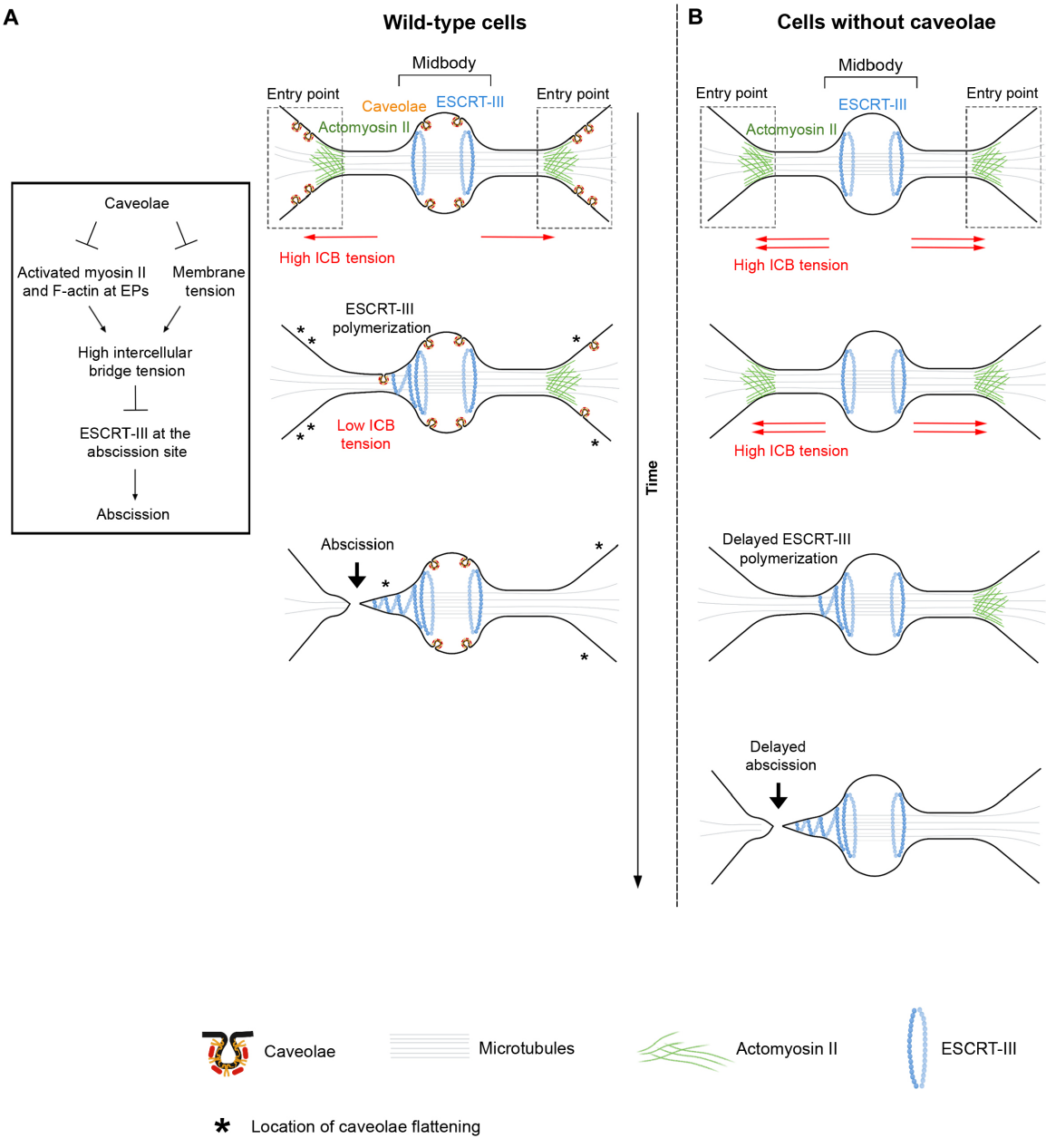

Fig. 6. Model: Caveolae buffer ICB tension by limiting the F-actin/myosin II–dependent contractility and membrane tension, thereby promoting ESCRT-III polymerization and successful abscission. (**A**) Cells with caveolae (WT cells). Box: Proposed mechanism for the control of abscission by caveolae. (**B**) Cells without caveolae (e.g., Cavin1 KO cells).

would then promote ESCRT-III polymerization at the abscission site and thus abscission. In agreement with the idea that caveolae flattening at EPs reduces ICB tension, it is known that ESCRT-III starts to polymerize as a cone at the presumptive abscission site approximately 30 min before abscission occurs, and this corresponds to the time when caveolae at the EP intensity reach a minimum (Fig. 2B). Interestingly, previous quantitative measurements showed that the tension at the ICB also diminishes at that time (*14*). In addition, we observed that abscission preferentially occurred on the side where the EP had the highest caveolae intensity ($P = 0.04$, Pearson χ^2 test). Time-lapse microscopy indicated that the first microtubule cut at the ICB occurred on the same side as EP1 (see Fig. 2B, Cavin1 intensity at EP1 > EP2) in 14 of 20 cases analyzed (70%). This raises the possibility that the asymmetric distribution of caveolae at EPs could favor ESCRT-III polymerization on a specific side of the ICB. Nevertheless, it is likely that other factors, such as the position of the older centriole (*67*, *68*), contribute to determine on which side of the midbody the first abscission occurs. Beside caveolae flattening at EPs, caveolae flattening at the plasma membrane of the daughter cells, outside the EP regions, could also contribute to the reduction of ICB tension that precedes abscission. In addition, the flattening of the caveolae localized at (or close to) the tip of the ESCRT-III cone (Fig. 2, C and D) could also help the constriction of the plasma membrane at the abscission site by locally reducing membrane tension.

Second, caveolae at EPs could also negatively regulate acto-myosin II–dependent contractility at or close to the ICB. Depleting Cavin1 leads to an increase of the proportion of ICBs with activated myosin II at EPs, associated with a twofold increase in ICB tension (Fig. 4, B and D). This regulation appears local, since global myosin II activation during cytokinesis is unchanged after caveolae depletion (fig. S6B). Furthermore, pharmacological inhibition of ROCK in Cavin1 KO cells enabled to restore both normal pMRLC patterns at the EPs and normal ICB tension (Fig. 5, A and B). This suggests that the abnormally high ICB tension observed after caveolae loss results from the local increase in acto-myosin II activity at the EPs. All our data (Figs. 4, C and D, and 5, A to D, and fig. S9C) indicate that ICBs, where pMRLC is accumulated at both EPs, are more tensed than ICBs displaying no accumulation of pMRLC at EPs. How the presence of caveolae at EPs seen in WT cells locally regulates this previously undescribed pool of activated myosin II to restrict ICB tension is not known and would require future investigation. This phenomenon was not associated with an activation of the abscission checkpoint (fig. S7, A to D). Nonetheless, the inverse correlation between high levels of activated myosin II and high levels of Cavin1 at EPs, both at local (Fig. 4, E and F, and fig. S8A) and EP scales (fig. S8B), is remarkable and might involve complex biochemical reciprocal inhibitory signals between caveolae and the acto-myosin system. There is increasing evidence that caveolae regulate both membrane tension and acto-myosin II activity at the plasma membrane (*27*, *69*–*72*), in particular during rear-to-front retraction during durotaxis-mediated migration (*71*) and in cell-cell contacts involved in melanin pigment transfer from melanocytes to keratinocytes (*72*). Furthermore, caveolae have been recently implicated in the negative regulation of F-actin polymerization and thereby intercellular tension through adherens junctions between nondividing epithelial cells (*27*). The parallel with the role of caveolae as a negative regulator of ICB tension during cell division is striking, although the functional consequence—ESCRT-III polymerization and membrane scission—is very different. Thus, the local regulation of acto-myosin–dependent contractility coupled to the buffering of membrane tension might represent a general function of caveolae.

To conclude, we propose the following model to explain the interplay between caveolae, myosin II activation at EPs, ICB tension, and ESCRT-III polymerization and abscission (Fig. 6). In WT context (Fig. 6A), the dividing cells pull on their ICBs while they spread in late telophase, as previously described (*14*). This likely explains why activated myosin II accumulates at EPs and thus maintains high tension at the ICB at this stage of cytokinesis (Fig. 6A, top drawing), since applying forces on the membrane generally induces the local recruitment of activated myosin II at the cortex under tension (*73*). However, the presence of caveolae at EPs and at the abscission site buffers this high membrane tension and consequently limits myosin II activation at the ICB (Fig. 6A, middle drawing). This promotes a decrease of the ICB tension, thus favoring the polymerization of ESCRT-III at the abscission site to allow abscission (Fig. 6A, bottom drawing). In cells without caveolae (Fig. 6B), the lack of the caveolae membrane reservoir and the abnormally high activation of myosin II at EPs lead to an unregulated and abnormal increase in ICB tension that is detrimental for ESCRT-III polymerization and abscission. This could be particularly relevant in tumorigenesis, since caveolae both promote elimination of cancer cells through extrusion (*27*) and prevent the formation of binucleated cells (this study), a well-established starting point for tumor formation (*74*, *75*). The unexpected connection between caveolae and the ESCRT machinery should also stimulate investigation on how caveolae might control other key ESCRT-III–dependent processes beyond cell division, such as the budding of enveloped viruses and plasma membrane repair.

MATERIALS AND METHODS

Cell culture

HeLa CCL-2 (American Type Culture Collection), HeLa Control KO [HeLa CCL-2 transfected with a plasmid encoding Cas9 without guide RNA (gRNA) described in (*38*)], HeLa Cavin1 KO [HeLa CCL-2 transfected with a plasmid encoding Cas9 and a gRNA targeting *Cavin1* described in (*38*)], and HeLa CHMP4B-GFP described in (*37*) were grown in Dulbecco's modified Eagle's medium (DMEM) GlutaMAX (Gibco, Invitrogen Life Technologies, #31966). All culture media were supplemented with 10% fetal bovine serum (FBS; Dutscher, #500105R1) and 1% penicillin/streptomycin (Gibco, #15140122) and cultured in 5% CO_2 condition at 37°C. CHMP4B-GFP stable cell lines were generated by lentiviral transduction of HeLa Control KO and Cavin1 KO cells and selected by flow cytometry [fluorescence-activated cell sorting (FACS)] sorting. A Cavin1-NG (mNeonGreen) stable cell line was generated by lentiviral transduction of HeLa cells and selected by flow cytometry (FACS) sorting. For the ROCK inhibitor experiments, HeLa Control KO and Cavin1 KO were treated with Y27632 (Calbiochem) at 20 μM overnight (Fig. 5, B and D), 50 μM for 3 hours (Fig. 5, A and C), or 50 μM for 2 hours after a mitotic shake-replate of 2 hours (fig. S8C).

Plasmid constructs

Cavin1-GFP and Cav1-RFP were described previously in (*76*). To construct Cavin1-mApple, the Cavin1 coding sequence from complementry DNA was subcloned into Gateway pENTR plasmids. The transient expression vector was generated by recombination

(Thermo Fisher Scientific) of Cavin1-pENTR and pDEST mApple N1. The plasmid encoding GFP-Rab35 was described in (*77*).

Cell transfections and siRNAs

For live cell imaging, HeLa cells were transfected with 200 ng of plasmids for 48 hours using X-tremeGENE 9 DNA reagent (Roche; Fig. 2A) or electroporated with 2 μg of plasmid using Lonza's nucleofection protocol (fig. S3A). For the fast acquisition movies, HeLa cells were transfected with a total of 150 ng of plasmids encoding Cavin1-GFP and Cav1-RFP using X-tremeGENE 9 DNA reagent (fig. S3B). HeLa CHMP4B-GFP cells were transfected with 80 ng of plasmids encoding Cavin1-mApple for 48 hours using X-tremeGENE 9 DNA reagent (Fig. 2D). HeLa cells were transfected with 100 ng of plasmids encoding GFP-Rab35 for 24 hours using X-tremeGENE 9 DNA reagent (fig. S2B). For the rescue experiments, Control KO and Cavin1 KO cells were transfected with 200 ng of plasmids for 24 hours (fig. S5A) or with 120 ng of plasmids [Histone2B-RFP (40 ng) + Empty (80 ng) or Histone2B-RFP (40 ng) + Cavin1 WT (80 ng) plasmids] for 24 hours (Fig. 3, C and F), using X-tremeGENE 9 DNA reagent (Roche).

Depletion of Cav1 (fig. S5 B, C) was achieved by RNA interference using siRNAs with the following sequence: 5′-GCAUCAACUUGCAGAAAGA-3′ (Merck), and Control siRNA Luciferase: 5′-CGUACGCGGAAUACUUCGA-3′ (Merck). HeLa cells were transfected on two consecutive days with 20 nM Cav1 siRNAs using Lipofectamine RNAiMAX (Invitrogen), following the manufacturer's instructions, and recorded 3 days later.

Western blots

siRNA-treated HeLa cells and Control KO and Cavin1 KO cells were directly lysed in 1x Laemmli (Bio-Rad Laboratories) with Benzonase nuclease (Millipore, #70664) and migrated in 10% SDS–polyacrylamide gel electrophoresis (SDS-PAGE) gels (Bio-Rad Laboratories). Control KO and Cavin1 KO cells used in the rescue experiments were detached with trypsin (Gibco), collected, and lysed with NP-40 extract buffer [50 mM tris (pH 8), 150 mM NaCl, and 1% NP-40] containing protease inhibitors (Roche, #11873580001), and 30 μg of lysate was migrated in 10% SDS-PAGE gels (Bio-Rad Laboratories). In both cases, the migrated gels were transferred onto polyvinylidene difluoride membranes (Millipore) and incubated overnight at 4°C with corresponding primary antibodies (table S1) in 50 mM tris-HCl (pH 8.0), 150 mM NaCl, 0.1% Tween 20, and 5% milk. This was followed by incubation with horseradish peroxidase (HRP)–coupled secondary antibodies (1:10,000; Jackson ImmunoResearch) for 1 hour at room temperature (RT) and revealed by chemiluminescence using Immobilon Crescendo or Forte Western HRP substrate (Millipore Merck).

For Western blots against pMRLC, MRLC, and actin, cells were lysed with 1× Laemmli (Bio-Rad Laboratories) with Benzonase nuclease and phosphatase inhibitors (Sigma-Aldrich p2850, Merck), and the lysates were migrated in 4 to 15% gradient SDS-PAGE gels (Bio-Rad Laboratories). Gels were transferred onto nitrocellulose membranes (Whatman Protran) and incubated overnight with primary antibodies in 50 mM tris-HCl (pH 8.0), 150 mM NaCl, 0.1% Tween 20, and 5% bovine serum albumin (BSA). Fluorescently coupled secondary antibodies (1:10,000; Jackson ImmunoResearch) were incubated for 30 min in tris-HCl (pH 8.0), 150 mM NaCl, 0.1% Tween 20, and 3% milk at RT and revealed by LI-COR Biosciences.

Immunofluorescence and image acquisition

MBRs were purified as described in (*37*) and fixed with pure methanol (Sigma-Aldrich, #32213) at −20°C for 3 min. HeLa cells were grown on coverslips and fixed with either 4% paraformaldehyde (PFA; Sigma-Aldrich, #15714) for 20 min (table S1) or pure methanol (Sigma-Aldrich, #32213) at −20°C for 3 min (table S1). Cells and MBRs were permeabilized with 0.1% Triton X-100 and blocked with phosphate-buffered saline (PBS) containing 1% BSA for 1 hour at RT and then incubated with the corresponding primary antibodies (table S1) diluted in PBS containing 1% BSA for 1 to 2 hours at RT. This was followed by an incubation with the secondary antibodies diluted in PBS containing 1% BSA for 1 hour at RT. DyLight 405–, DyLight Alexa 488–, and Cy3- and Cy5-conjugated secondary antibodies (The Jackson Laboratory) were diluted 1:1000. Cells were additionally stained with 4′,6-diamidino-2-phenylindole (0.5 mg/ml; Serva) for 5 min at RT. For visualization of pCHMP4C at the midbody, the staining was done as described in (*13*). For visualization of pppCHMP4C in ACBs, cells were pre-permeabilized and stained as described in (*51*). Cells and MBRs were finally mounted in Mowiol (Calbiochem). Image acquisition was done with an inverted Eclipse Nikon Ti-E microscope, using a 100× 1.4 numerical aperture (NA) PL-APO objective lens or a 60× 1.4 NA PL-APO VC objective lens, coupled to a charge-coupled device (CCD) camera (Photometrics CoolSNAP HQ) or Retiga R6 CCD camera (Teledyne Photometrics) and MetaMorph software (MDS), or using a CSU-X1 spinning disk confocal scanning unit (Yokogawa) coupled to a Prime 95S scientific complementary metal-oxide semiconductor (sCMOS) camera (Teledyne Photometrics) and CSU 100× objective. Images were then converted into 8-bit images using Fiji software (National Institutes of Health) and mounted in Photoshop CS6.

Osmotic shock experiments

Mild hyper-osmotic shocks were performed as in (*65*). A total of 30,000 cells were seeded on glass coverslips the day before the experiment and treated for 90 min either with isotonic cultured medium (DMEM, 10% FBS, 300 mOsm) or with DMEM and 10% FBS medium containing D-glucose (Sigma-Aldrich, #G5767) to obtain a final osmotic pressure of 400 mOsm. Cells were then fixed and immunostained.

Time-lapse microscopy

For time-lapse phase-contrast imaging (abscission times), 30,000 cells were plated on glass-bottom 12-well plates (MatTek) 2 days before recording, incubated in an open chamber (Life Imaging) equilibrated in 5% CO_2, and maintained at 37°C. In the case of high and low confluency conditions (Fig. 5E), 100,000 and 10,000 trypsinized cells, respectively, were replated on glass-bottom 12-well plates for 3 hours. The culture medium was then changed, and SiR-tubulin was added for 1 hour before recording. Time-lapse sequences were recorded every 10 min for 48 hours using an inverted Nikon Eclipse Ti-E microscope with a 20× 0.45 NA Plan Fluor ELWD controlled by MetaMorph software (Universal Imaging).

For time-lapse fluorescent imaging, images were acquired using an inverted Nikon Eclipse Ti-E microscope equipped with a CSU-X1 spinning disk confocal scanning unit (Yokogawa) and with an electron-multiplying CCD (EMCCD) camera (Evolve 512 Delta, Photometrics) or a Prime 95S sCMOS camera (Teledyne Photometrics). Images were acquired with CSU 100× or CSU 60× 1.4 NA PL-APO VC objectives and MetaMorph software (MDS). For fig. S3B, images were acquired at 1-min intervals with Z-stacks (0.7 μm between

Z-planes) for 3 hours. Cavin1 dots were manually tracked with ImageJ and analyzed from the Z-planes with the highest fluorescence intensities.

Laser ablation

Laser ablation experiments were performed using a pulsed 355-nm UV laser (Roper Scientific) controlled by MetaMorph and the iLas2 system (GATACA systems). The laser ablation system was connected to an inverted Nikon Eclipse Ti microscope confocal spinning disk equipped with a Yokagawa CSU-X1 spinning head, coupled to an EMCCD camera (Evolve, Photometrics) and a 100× objective (Nikon S Fluor 100× 0.5 to 1.3 NA). The 355-nm UV laser is sufficient for membrane and microtubule cut, as described and demonstrated in (*14*). To record the movement of the midbody following laser ablation, fast acquisition movies (20-ms time lapse) were made using only transmitted light. The displacement of the midbody was then tracked using the software Icy (*78*). The midbody displacement after laser ablation follows a double-exponential function as described in (*14*), and the retraction speed of the midbody was obtained from a linear regression of the first hundreds of milliseconds after ablation.

Cell synchronization

For EM and Western blots for detecting pMRLC, MRLC, and actin, a mitotic shake-off was performed to select the cells in mitosis. Two days before the experiment, 2 million HeLa cells were seeded in T75 flasks. First, mitotic and dead cells were shaken off and the remaining cells were further incubated for 2 hours with fresh filtered medium (DMEM GlutaMAX supplemented with 10% FBS and 1% penicillin/streptomycin). Cells were again shaken off, and the supernatant containing the mitotic cells was collected and centrifuged (900*g* for 3 min) in 15-ml tubes. The pellet of cells was then resuspended and added to collagen I (Gibco, #A10483)–coated glass coverslips (50 μg/ml, for EM) and p6-well plate (50 μg/ml, for Western blots) and then incubated for 1 and 2 hours, respectively, at 5% CO_2 and 37°C to allow them to exit mitosis synchronously and to progress into cytokinesis. For fig. S8C, 80,000 mitotic-shaken cells were plated on p24-well plates for 2 hours and then treated for an additional 2 hours with Y27632 (50 μg/ml) before fixation.

Electron microscopy

Glass coverslips with synchronized cytokinetic cells were chemically fixed for 2 hours at RT in cacodylate buffer (0.1 M, pH 7.2) supplemented with 2.5% (v/v) glutaraldehyde and 2% (v/v) PFA, then washed in cacodylate buffer (three times), postfixed with 2% (w/v) osmium tetroxide supplemented with 1.5% (w/v) potassium ferrocyanide (45 min for 4°C), washed in water (three times), dehydrated in ethanol (increasing concentration from 30 to 100%), and finally embedded in Embed812/Araldite (Epon) resin as described in (*79*). Microtomy of embedded cell monolayers was performed on a Reichert UltraCut S ultramicrotome (Leica Microsystems) for 70-nm-thin sections collected on formvar-coated cupper/palladium grids and then contrasted with uranyl acetate and lead citrate. Electron micrographs were acquired with a TEM (Tecnai Spirit G2; Thermo Fisher Scientific, Eindhoven, The Netherlands) equipped with a 4k CCD camera (Quemesa, EMSIS, Muenster, Germany) using ITEM software (EMSIS).

Image and data analyses

All images and videos were minimally processed to adjust the intensity levels, reduce image noise, and rotate the images with Fiji software. The kymographs (Fig. 4B) were obtained using a region of interest (ROI; straight line) along the ICB at a fixed position over the entire movie, using Icy software. The scan lines were obtained using an ROI (straight line), with a width corresponding to the bridge or EP height, along the objects of interest, using Fiji. Pixel intensity values were extracted from the EPs defined with an ROI (square) for each channel of interest, using Fiji. Illustrations were created with BioRender.com.

Statistical analyses

All the plots and statistical tests were performed using GraphPad Prism software. The presented values are displayed as mean ± SD for at least three independent experiments (as indicated in the figure legends). The significance was calculated using unpaired, one-sided/two-sided *t* tests, as indicated. For comparing the distributions of the abscission times, a nonparametric and distribution-free Kolmogorov-Smirnov test was used. In all statistical tests, $P > 0.05$ was considered as nonsignificant. *P* values are indicated in the figures.

SUPPLEMENTARY MATERIALS

Supplementary material for this article is available at https://science.org/doi/10.1126/sciadv.abm5095

View/request a protocol for this paper from *Bio-protocol*.

REFERENCES AND NOTES

1. B. Mierzwa, D. W. Gerlich, Cytokinetic abscission: Molecular mechanisms and temporal control. *Dev. Cell* **31**, 525–538 (2014).
2. C. Addi, J. Bai, A. Echard, Actin, microtubule, septin and ESCRT filament remodeling during late steps of cytokinesis. *Curr. Opin. Cell Biol.* **50**, 27–34 (2018).
3. D. Dambournet, M. Machicoane, L. Chesneau, M. Sachse, M. Rocancourt, A. el Marjou, E. Formstecher, R. Salomon, B. Goud, A. Echard, Rab35 GTPase and OCRL phosphatase remodel lipids and F-actin for successful cytokinesis. *Nat. Cell Biol.* **13**, 981–988 (2011).
4. J. A. Schiel, G. C. Simon, C. Zaharris, J. Weisz, D. Castle, C. C. Wu, R. Prekeris, FIP3-endosome-dependent formation of the secondary ingression mediates ESCRT-III recruitment during cytokinesis. *Nat. Cell Biol.* **14**, 1068–1078 (2012).
5. S. Frémont, H. Hammich, J. Bai, H. Wioland, K. Klinkert, M. Rocancourt, C. Kikuti, D. Stroebel, G. Romet-Lemonne, O. Pylypenko, A. Houdusse, A. Echard, Oxidation of F-actin controls the terminal steps of cytokinesis. *Nat. Commun.* **8**, 14528 (2017).
6. S. Fremont, A. Echard, Membrane traffic in the late steps of cytokinesis. *Curr. Biol.* **28**, R458–R470 (2018).
7. S. J. Terry, F. Dona, P. Osenberg, J. G. Carlton, U. S. Eggert, Capping protein regulates actin dynamics during cytokinetic midbody maturation. *Proc. Natl. Acad. Sci. U.S.A.* **115**, 2138–2143 (2018).
8. F. Niu, K. Sun, W. Wei, C. Yu, Z. Wei, F-actin disassembly factor MICAL1 binding to Myosin Va mediates cargo unloading during cytokinesis. *Sci. Adv.* **6**, eabb1307 (2020).
9. N. V. G. Iannantuono, G. Emery, Rab11FIP1 maintains Rab35 at the intercellular bridge to promote actin removal and abscission. *J. Cell Sci.* **134**, jcs244384 (2021).
10. J. G. Carlton, J. Martin-Serrano, Parallels between cytokinesis and retroviral budding: A role for the ESCRT machinery. *Science* **316**, 1908–1912 (2007).
11. E. Morita, V. Sandrin, H. Y. Chung, S. G. Morham, S. P. Gygi, C. K. Rodesch, W. I. Sundquist, Human ESCRT and ALIX proteins interact with proteins of the midbody and function in cytokinesis. *EMBO J.* **26**, 4215–4227 (2007).
12. P. P. D'Avino, L. Capalbo, Regulation of midbody formation and function by mitotic kinases. *Semin. Cell Dev. Biol.* **53**, 57–63 (2016).
13. L. Capalbo, I. Mela, M. A. Abad, A. A. Jeyaprakash, J. M. Edwardson, P. P. D'Avino, Coordinated regulation of the ESCRT-III component CHMP4C by the chromosomal passenger complex and centralspindlin during cytokinesis. *Open Biol.* **6**, 160248 (2016).
14. J. Lafaurie-Janvore, P. Maiuri, I. Wang, M. Pinot, J. B. Manneville, T. Betz, M. Balland, M. Piel, ESCRT-III assembly and cytokinetic abscission are induced by tension release in the intercellular bridge. *Science* **339**, 1625–1629 (2013).
15. R. G. Parton, Caveolae: Structure, function, and relationship to disease. *Annu. Rev. Cell Dev. Biol.* **34**, 111–136 (2018).
16. R. G. Parton, M. del Pozo, S. Vassilopoulos, I. R. Nabi, S. le Lay, R. Lundmark, A. K. Kenworthy, A. Camus, C. M. Blouin, W. C. Sessa, C. Lamaze, Caveolae: The FAQs. *Traffic* **21**, 181–185 (2020).

17. R. G. Parton, V. Tillu, K. A. McMahon, B. M. Collins, Key phases in the formation of caveolae. *Curr. Opin. Cell Biol.* **71**, 7–14 (2021).
18. N. Ariotti, M. A. Fernández-Rojo, Y. Zhou, M. M. Hill, T. L. Rodkey, K. L. Inder, L. B. Tanner, M. R. Wenk, J. F. Hancock, R. G. Parton, Caveolae regulate the nanoscale organization of the plasma membrane to remotely control Ras signaling. *J. Cell Biol.* **204**, 777–792 (2014).
19. P. Sens, M. S. Turner, Budded membrane microdomains as tension regulators. *Phys. Rev. E Stat. Nonlinear Soft Matter Phys.* **73**, 031918 (2006).
20. B. Sinha, D. Köster, R. Ruez, P. Gonnord, M. Bastiani, D. Abankwa, R. V. Stan, G. Butler-Browne, B. Vedie, L. Johannes, N. Morone, R. G. Parton, G. Raposo, P. Sens, C. Lamaze, P. Nassoy, Cells respond to mechanical stress by rapid disassembly of caveolae. *Cell* **144**, 402–413 (2011).
21. O. L. Gervásio, W. D. Phillips, L. Cole, D. G. Allen, Caveolae respond to cell stretch and contribute to stretch-induced signaling. *J. Cell Sci.* **124**, 3581–3590 (2011).
22. M. A. Del Pozo, F. N. Lolo, A. Echarri, Caveolae: Mechanosensing and mechanotransduction devices linking membrane trafficking to mechanoadaptation. *Curr. Opin. Cell Biol.* **68**, 113–123 (2021).
23. H. P. Lo, S. J. Nixon, T. E. Hall, B. S. Cowling, C. Ferguson, G. P. Morgan, N. L. Schieber, M. A. Fernandez-Rojo, M. Bastiani, M. Floetenmeyer, N. Martel, J. Laporte, P. F. Pilch, R. G. Parton, The caveolin-cavin system plays a conserved and critical role in mechanoprotection of skeletal muscle. *J. Cell Biol.* **210**, 833–849 (2015).
24. J. Garcia, J. Bagwell, B. Njaine, J. Norman, D. S. Levic, S. Wopat, S. E. Miller, X. Liu, J. W. Locasale, D. Y. R. Stainier, M. Bagnat, Sheath cell invasion and trans-differentiation repair mechanical damage caused by loss of caveolae in the zebrafish notochord. *Curr. Biol.* **27**, 1982–1989.e3 (2017).
25. Y.-W. Lim, H. P. Lo, C. Ferguson, N. Martel, J. Giacomotto, G. A. Gomez, A. S. Yap, T. E. Hall, R. G. Parton, Caveolae protect notochord cells against catastrophic mechanical failure during development. *Curr. Biol.* **27**, 1968–1981.e7 (2017).
26. M. Dewulf, D. V. Köster, B. Sinha, C. Viaris de Lesegno, V. Chambon, A. Bigot, M. Bensalah, E. Negroni, N. Tardif, J. Podkalicka, L. Johannes, P. Nassoy, G. Butler-Browne, C. Lamaze, C. M. Blouin, Dystrophy-associated caveolin-3 mutations reveal that caveolae couple IL6/STAT3 signaling with mechanosensing in human muscle cells. *Nat. Commun.* **10**, 1974 (2019).
27. J. L. Teo, G. A. Gomez, S. Weeratunga, E. M. Davies, I. Noordstra, S. Budnar, H. Katsuno-Kambe, M. J. McGrath, S. Verma, V. Tomatis, B. R. Acharya, L. Balasubramaniam, R. M. Templin, K.-A. McMahon, Y. S. Lee, R. J. Ju, S. J. Stebhens, B. Ladoux, C. A. Mitchell, B. M. Collins, R. G. Parton, A. S. Yap, Caveolae control contractile tension for epithelia to eliminate tumor cells. *Dev. Cell* **54**, 75–91.e7 (2020).
28. V. Singh, C. Lamaze, Membrane tension buffering by caveolae: A role in cancer? *Cancer Metastasis Rev.* **39**, 505–517 (2020).
29. S. Matsumura, T. Kojidani, Y. Kamioka, S. Uchida, T. Haraguchi, A. Kimura, F. Toyoshima, Interphase adhesion geometry is transmitted to an internal regulator for spindle orientation via caveolin-1. *Nat. Commun.* **7**, ncomms11858 (2016).
30. E. Boucrot, M. T. Howes, T. Kirchhausen, R. G. Parton, Redistribution of caveolae during mitosis. *J. Cell Sci.* **124**, 1965–1972 (2011).
31. H. Kogo, T. Fujimoto, Concentration of caveolin-1 in the cleavage furrow as revealed by time-lapse analysis. *Biochem. Biophys. Res. Commun.* **268**, 82–87 (2000).
32. B. Feng, H. Schwarz, S. Jesuthasan, Furrow-specific endocytosis during cytokinesis of zebrafish blastomeres. *Exp. Cell Res.* **279**, 14–20 (2002).
33. N. Elia, R. Sougrat, T. A. Spurlin, J. H. Hurley, J. Lippincott-Schwartz, Dynamics of endosomal sorting complex required for transport (ESCRT) machinery during cytokinesis and its role in abscission. *Proc. Natl. Acad. Sci. U.S.A.* **108**, 4846–4851 (2011).
34. E. F. Crowell, J. Y. Tinevez, A. Echard, A simple model for the fate of the cytokinesis midbody remnant: Implications for remnant degradation by autophagy: Modeling remnant production and degradation enables re-interpretation of published data and improves design of future experiments. *Bioessays* **35**, 472–481 (2013).
35. E. F. Crowell, A. L. Gaffuri, B. Gayraud-Morel, S. Tajbakhsh, A. Echard, Engulfment of the Midbody remnant after cytokinesis in mammalian cells. *J. Cell Sci.* **127**, 3840–3851 (2014).
36. E. Peterman, P. Gibieža, J. Schafer, V. A. Skeberdis, A. Kaupinis, M. Valius, X. Heiligenstein, I. Hurbain, G. Raposo, R. Prekeris, The post-abscission midbody is an intracellular signaling organelle that regulates cell proliferation. *Nat. Commun.* **10**, 3181 (2019).
37. C. Addi, A. Presle, S. Frémont, F. Cuvelier, M. Rocancourt, F. Milin, S. Schmutz, J. Chamot-Rooke, T. Douché, M. Duchateau, Q. Giai Gianetto, A. Salles, H. Ménager, M. Matondo, P. Zimmermann, N. Gupta-Rossi, A. Echard, The Flemmingsome reveals an ESCRT-to-membrane coupling via ALIX/syntenin/syndecan-4 required for completion of cytokinesis. *Nat. Commun.* **11**, 1941 (2020).
38. C. Roffay, G. Molinard, K. Kim, M. Urbanska, V. Andrade, V. Barbarasa, P. Nowak, V. Mercier, J. García-Calvo, S. Matile, R. Loewith, A. Echard, J. Guck, M. Lenz, A. Roux, Passive coupling of membrane tension and cell volume during active response of cells to osmosis. *Proc. Natl. Acad. Sci. U.S.A.* **118**, e2103228118 (2021).
39. M. M. Hill, M. Bastiani, R. Luetterforst, M. Kirkham, A. Kirkham, S. J. Nixon, P. Walser, D. Abankwa, V. M. J. Oorschot, S. Martin, J. F. Hancock, R. G. Parton, PTRF-Cavin, a conserved cytoplasmic protein required for caveola formation and function. *Cell* **132**, 113–124 (2008).
40. L. Liu, D. Brown, M. McKee, N. K. LeBrasseur, D. Yang, K. H. Albrecht, K. Ravid, P. F. Pilch, Deletion of Cavin/PTRF causes global loss of caveolae, dyslipidemia, and glucose intolerance. *Cell Metab.* **8**, 310–317 (2008).
41. A. Echarri, D. M. Pavón, S. Sánchez, M. García-García, E. Calvo, C. Huerta-López, D. Velázquez-Carreras, C. Viaris de Lesegno, N. Ariotti, A. Lázaro-Carrillo, R. Strippoli, D. de Sancho, J. Alegre-Cebollada, C. Lamaze, R. G. Parton, M. A. del Pozo, An Abl-FBP17 mechanosensing system couples local plasma membrane curvature and stress fiber remodeling during mechanoadaptation. *Nat. Commun.* **10**, 5828 (2019).
42. P. Sens, J. Plastino, Membrane tension and cytoskeleton organization in cell motility. *J. Phys. Condens. Matter* **27**, 273103 (2015).
43. P. Steigemann, C. Wurzenberger, M. H. A. Schmitz, M. Held, J. Guizetti, S. Maar, D. W. Gerlich, Aurora B-mediated abscission checkpoint protects against tetraploidization. *Cell* **136**, 473–484 (2009).
44. J. Bai, H. Wioland, T. Advedissian, F. Cuvelier, G. Romet-Lemonne, A. Echard, Actin reduction by MsrB2 is a key component of the cytokinetic abscission checkpoint and prevents tetraploidy. *Proc. Natl. Acad. Sci. U.S.A.* **117**, 4169–4179 (2020).
45. M. Dandoulaki, E. Petsalaki, D. Sumpton, S. Zanivan, G. Zachos, Src activation by Chk1 promotes actin patch formation and prevents chromatin bridge breakage in cytokinesis. *J. Cell Biol.* **217**, 3071–3089 (2018).
46. E. Petsalaki, G. Zachos, The abscission checkpoint: A guardian of chromosomal stability. *Cells* **10**, 3350 (2021).
47. J. G. Carlton, A. Caballe, M. Agromayor, M. Kloc, J. Martin-Serrano, ESCRT-III governs the Aurora B-mediated abscission checkpoint through CHMP4C. *Science* **336**, 220–225 (2012).
48. S. B. Thoresen, C. Campsteijn, M. Vietri, K. O. Schink, K. Liestøl, J. S. Andersen, C. Raiborg, H. Stenmark, ANCHR mediates Aurora-B-dependent abscission checkpoint control through retention of VPS4. *Nat. Cell Biol.* **16**, 547–557 (2014).
49. A. Caballe, D. M. Wenzel, M. Agromayor, S. L. Alam, J. J. Skalicky, M. Kloc, J. G. Carlton, L. Labrador, W. I. Sundquist, J. Martin-Serrano, ULK3 regulates cytokinetic abscission by phosphorylating ESCRT-III proteins. *eLife* **4**, e06547 (2015).
50. R. Bhowmick, R. S. Thakur, A. B. Venegas, Y. Liu, J. Nilsson, M. Barisic, I. D. Hickson, The RIF1-PP1 axis controls abscission timing in human cells. *Curr. Biol.* **29**, 1232–1242.e5 (2019).
51. L. K. Williams, D. R. Mackay, M. A. Whitney, G. C. Couldwell, W. I. Sundquist, K. S. Ullman, Identification of abscission checkpoint bodies as structures that regulate ESCRT factors to control abscission timing. *eLife* **10**, e63743 (2021).
52. L. Capalbo, Z. I. Bassi, M. Geymonat, S. Todesca, L. Copoiu, A. J. Enright, G. Callaini, M. G. Riparbelli, L. Yu, J. S. Choudhary, E. Ferrero, S. Wheatley, M. E. Douglas, M. Mishima, P. P. D'Avino, The midbody interactome reveals unexpected roles for PP1 phosphatases in cytokinesis. *Nat. Commun.* **10**, 4513 (2019).
53. A. Rai, D. W. Greening, R. Xu, M. Chen, W. Suwakulsiri, R. J. Simpson, Secreted midbody remnants are a class of extracellular vesicles molecularly distinct from exosomes and microparticles. *Commun. Biol.* **4**, 400 (2021).
54. A. Presle, S. Frémont, A. Salles, P.-H. Commere, N. Sassoon, C. Berlioz-Torrent, N. Gupta-Rossi, A. Echard, The viral restriction factor tetherin/BST2 tethers cytokinetic midbody remnants to the cell surface. *Curr. Biol.* **31**, 2203–2213.e5 (2021).
55. J. M. Mullins, J. J. Biesele, Terminal phase of cytokinesis in D-98s cells. *J. Cell Biol.* **73**, 672–684 (1977).
56. J. A. Schiel, K. Park, M. K. Morphew, E. Reid, A. Hoenger, R. Prekeris, Endocytic membrane fusion and buckling-induced microtubule severing mediate cell abscission. *J. Cell Sci.* **124**, 1411–1424 (2011).
57. J. Guizetti, L. Schermelleh, J. Mäntler, S. Maar, I. Poser, H. Leonhardt, T. Müller-Reichert, D. W. Gerlich, Cortical constriction during abscission involves helices of ESCRT-III-dependent filaments. *Science* **331**, 1616–1620 (2011).
58. E. Kettle, S. L. Page, G. P. Morgan, C. S. Malladi, C. L. Wong, R. A. Boadle, B. J. Marsh, P. J. Robinson, M. Chircop, A cholesterol-dependent endocytic mechanism generates midbody tubules during cytokinesis. *Traffic* **16**, 1174–1192 (2015).
59. G. E. Atilla-Gokcumen, E. Muro, J. Relat-Goberna, S. Sasse, A. Bedigian, M. L. Coughlin, S. Garcia-Manyes, U. S. Eggert, Dividing cells regulate their lipid composition and localization. *Cell* **156**, 428–439 (2014).
60. C. Cauvin, A. Echard, Phosphoinositides: Lipids with informative heads and mastermind functions in cell division. *Biochim. Biophys. Acta* **1851**, 832–843 (2015).
61. U. Ortegren, M. Karlsson, N. Blazic, M. Blomqvist, F. H. Nystrom, J. Gustavsson, P. Fredman, P. Stralfors, Lipids and glycosphingolipids in caveolae and surrounding plasma membrane of primary rat adipocytes. *Eur. J. Biochem.* **271**, 2028–2036 (2004).
62. M. Hubert, E. Larsson, N. V. G. Vegesna, M. Ahnlund, A. I. Johansson, L. W. K. Moodie, R. Lundmark, Lipid accumulation controls the balance between surface connection and scission of caveolae. *eLife* **9**, e55038 (2020).

63. Y. Zhou, N. Ariotti, J. Rae, H. Liang, V. Tillu, S. Tee, M. Bastiani, A. T. Bademosi, B. M. Collins, F. A. Meunier, J. F. Hancock, R. G. Parton, Caveolin-1 and cavin1 act synergistically to generate a unique lipid environment in caveolae. *J. Cell Biol.* **220**, e202005138 (2021).
64. M. Y. Hein, N. C. Hubner, I. Poser, J. Cox, N. Nagaraj, Y. Toyoda, I. A. Gak, I. Weisswange, J. Mansfeld, F. Buchholz, A. A. Hyman, M. Mann, A human interactome in three quantitative dimensions organized by stoichiometries and abundances. *Cell* **163**, 712–723 (2015).
65. V. Mercier, J. Larios, G. Molinard, A. Goujon, S. Matile, J. Gruenberg, A. Roux, Endosomal membrane tension regulates ESCRT-III-dependent intra-lumenal vesicle formation. *Nat. Cell Biol.* **22**, 947–959 (2020).
66. L. Pelkmans, M. Zerial, Kinase-regulated quantal assemblies and kiss-and-run recycling of caveolae. *Nature* **436**, 128–133 (2005).
67. M. Piel, J. Nordberg, U. Euteneuer, M. Bornens, Centrosome-dependent exit of cytokinesis in animal cells. *Science* **291**, 1550–1553 (2001).
68. T. C. Kuo, C. T. Chen, D. Baron, T. T. onder, S. Loewer, S. Almeida, C. M. Weismann, P. Xu, J. M. Houghton, F. B. Gao, G. Q. Daley, S. Doxsey, Midbody accumulation through evasion of autophagy contributes to cellular reprogramming and tumorigenicity. *Nat. Cell Biol.* **13**, 1214–1223 (2011).
69. A. Grande-García, A. Echarri, J. de Rooij, N. B. Alderson, C. M. Waterman-Storer, J. M. Valdivielso, M. A. del Pozo, Caveolin-1 regulates cell polarization and directional migration through Src kinase and Rho GTPases. *J. Cell Biol.* **177**, 683–694 (2007).
70. A. Echarri, M. A. Del Pozo, Caveolae—Mechanosensitive membrane invaginations linked to actin filaments. *J. Cell Sci.* **128**, 2747–2758 (2015).
71. J. H. R. Hetmanski, H. de Belly, I. Busnelli, T. Waring, R. V. Nair, V. Sokleva, O. Dobre, A. Cameron, N. Gauthier, C. Lamaze, J. Swift, A. D. Campo, T. Starborg, T. Zech, J. G. Goetz, E. K. Paluch, J.-M. Schwartz, P. T. Caswell, Membrane tension orchestrates rear retraction in matrix-directed cell migration. *Dev. Cell* **51**, 460–475.e10 (2019).
72. L. Domingues, I. Hurbain, F. Gilles-Marsens, J. Sirés-Campos, N. André, M. Dewulf, M. Romao, C. Viaris de Lesegno, A. S. Macé, C. Blouin, C. Guéré, K. Vié, G. Raposo, C. Lamaze, C. Delevoye, Coupling of melanocyte signaling and mechanics by caveolae is required for human skin pigmentation. *Nat. Commun.* **11**, 2988 (2020).
73. J. C. Effler, Y. S. Kee, J. M. Berk, M. N. Tran, P. A. Iglesias, D. N. Robinson, Mitosis-specific mechanosensing and contractile-protein redistribution control cell shape. *Curr. Biol.* **16**, 1962–1967 (2006).
74. T. Fujiwara, M. Bandi, M. Nitta, E. V. Ivanova, R. T. Bronson, D. Pellman, Cytokinesis failure generating tetraploids promotes tumorigenesis in p53-null cells. *Nature* **437**, 1043–1047 (2005).
75. S. M. A. Lens, R. H. Medema, Cytokinesis defects and cancer. *Nat. Rev. Cancer* **19**, 32–45 (2019).
76. D. K. Sharma, J. C. Brown, A. Choudhury, T. E. Peterson, E. Holicky, D. L. Marks, R. Simari, R. G. Parton, R. E. Pagano, Selective stimulation of caveolar endocytosis by glycosphingolipids and cholesterol. *Mol. Biol. Cell* **15**, 3114–3122 (2004).
77. C. Cauvin, M. Rosendale, N. Gupta-Rossi, M. Rocancourt, P. Larraufie, R. Salomon, D. Perrais, A. Echard, Rab35 GTPase triggers switch-like recruitment of the Lowe syndrome lipid phosphatase OCRL on newborn endosomes. *Curr. Biol.* **26**, 120–128 (2016).
78. F. de Chaumont, S. Dallongeville, N. Chenouard, N. Hervé, S. Pop, T. Provoost, V. Meas-Yedid, P. Pankajakshan, T. Lecomte, Y. le Montagner, T. Lagache, A. Dufour, J. C. Olivo-Marin, Icy: An open bioimage informatics platform for extended reproducible research. *Nat. Methods* **9**, 690–696 (2012).
79. I. Hurbain, M. Romao, P. Bergam, X. Heiligenstein, G. Raposo, Analyzing lysosome-related organelles by electron microscopy. *Methods Mol. Biol.* **1594**, 43–71 (2017).

Acknowledgments: We dedicate this study to the memory of Dr M. Bornens, an outstanding cell biologist who made landmark discoveries in the centrosome, cytoskeleton and cell division fields. We thank M. Piel and the Echard Laboratory members for critical reading of the manuscript; M. Piel, A. Roux, and P. Sens for helpful discussions throughout this project; P. D'Avino for reagents; and the Recombinant antibodies platform (TAb-IP, Institut Curie, Paris) for antibodies and reagents. We thank A. Presle and N. Sassoon for the preparation of purified midbody remnants. We thank A. Salles from UTechS PBI, Institute Pasteur for discussions and advice in image acquisition; M. Moya-Nilges from UTechS PBI, Institute Pasteur for SEM training and help in image acquisition; Q. Giai Gianetto for making fig. S1B and for sharing his expertise in statistics; P.-H. Commere from Cytometry and Biomarkers Utechs, Institut Pasteur for FACS sorting; and V. Fraisier, the Cell and Tissue Imaging facility (PICT-IBiSA), and the Nikon Imaging Centre @ Institut Curie-CNRS for laser ablation experiments. **Funding:** This work was supported by Institut Pasteur (A.E.); CNRS (A.E.); ANR Cytosign, ANR SeptScort (A.E.); ANR MOTICAV (C.L.); ANR CAV-SM (C.L.); Fondation pour le Recherche Médicale: Recherche soutenue par la FRM EQU202103012627 (A.E.); French National Research Agency through the "Investments for the Future" program, France-BioImaging, ANR-10-INSB-04 (C.D.); Cell and Tissue Imaging core facility (PICT-IBiSA), member of the France-BioImaging national research infrastructure, supported by the Labex Cell(n)Scale (ANR-10-LBX-0038) part of the IDEX PSL (ANR-10-IDEX-0001-02 PSL) (C.D. and C.L.); Doctoral School Complexité du Vivant ED515, contrat n° 2828/2017 (V.A.); La Ligue Contre le Cancer (4ème année de thèse) (V.A.); Pasteur-Paris University (PPU) international PhD program (J.B.); Fondation ARC pour la recherche sur le cancer (DOC20180507410) (J.B.); Programme Labellisé PGA1-RF20170205456 (C.L.); and CEFIPRA, project 6301-1. **Author contributions:** V.A. carried out and analyzed all the experiments except mentioned otherwise. C.D. performed, analyzed, and interpreted the electron microscopy imaging experiments. J.B. obtained initial observations for Cavin1 localization. A.J. taught laser ablation experiments to V.A. N.G.-R. obtained initial data of the Flemmingsome. V.A., C.D., C.L., and A.E. designed the experiments. A.E. secured funding and analyzed and supervised the work. V.A. and A.E. wrote the manuscript with the help of C.L. and C.D. **Competing interests:** The authors declare that they have no competing interests. **Data and materials availability:** All data needed to evaluate the conclusions in the paper are present in the paper and/or the Supplementary Materials.

Submitted 22 September 2021
Accepted 15 February 2022
Published 13 April 2022
10.1126/sciadv.abm5095

ScienceAdvances

Caveolae promote successful abscission by controlling intercellular bridge tension during cytokinesis

Virginia AndradeJian BaiNeetu Gupta-RossiAna Joaquina JimenezCédric DelevoyeChristophe LamazeArnaud Echard

Sci. Adv., 8 (15), eabm5095. • DOI: 10.1126/sciadv.abm5095

Science Advances (ISSN) is published by the American Association for the Advancement of Science. 1200 New York Avenue NW, Washington, DC 20005. The title *Science Advances* is a registered trademark of AAAS.